NASA TR R-243

A THEORETICAL INVESTIGATION OF SIMULATION IN EXPANSION TUBES AND TUNNELS

By Robert L. Trimpi

Langley Research Center
Langley Station, Hampton, Va.

NATIONAL AERONAUTICS AND SPACE ADMINISTRATION

For sale by the Clearinghouse for Federal Scientific and Technical Information
Springfield, Virginia 22151 – Price $3.00

A THEORETICAL INVESTIGATION OF SIMULATION IN EXPANSION TUBES AND TUNNELS

By Robert L. Trimpi
Langley Research Center

SUMMARY

29068

A preliminary theoretical analysis was conducted of expansion-tube and expansion-tunnel simulation whereby the postnormal shock stagnation conditions of a model were matched to those of flight for both a perfect gas and equilibrium real air. The selected simulation mode permitted large variations from flight conditions for the test-section ambient temperature and pressure but only a small excursion for ambient velocity or density.

A brief treatment of the perfect-gas expansion tunnel with simulation demonstrated both gains and penalties in driver performance, depending on the Mach number, nozzle area ratio, driver gas, and simulation temperature ratio.

A more exhaustive analysis of an equilibrium real-air expansion tube employing simulation with ambient-gas temperatures of 1000° and 2000° K was completed for equivalent flight velocities from 20 000 to 50 000 feet per second (6.096 to 15.24 km/sec) and altitudes from 100 000 to 300 000 feet (30.48 to 91.44 km). The primary advantages of simulation were found to be large increases in testing time, initial test-gas slug length, and velocity-altitude performance. The primary disadvantages were a small degree of test-section dissociation and an increased peak cycle dissociation for the highest flow velocities and altitudes.

For equilibrium flow the gas state behind a shock wave was found to be closely simulated by all strong shock waves and to be well simulated even by weak waves with flow deflections as low as 30°.

Author

INTRODUCTION

The characteristics of expansion tubes and expansion tunnels operating to generate test-gas flows wherein the test medium exactly duplicates flight conditions have been reported in references 1 to 4. Certain advantages and disadvantages are obvious, and the question naturally arises as to means for reducing particular disadvantages without either a concurrent unacceptable reduction in advantages or the promotion of additional

disadvantages. The short testing time and the short initial extent of the test gas slug adjacent to the secondary diaphragm are two prime disadvantages of the expansion tube. One means of alleviating these particular drawbacks is the expansion tunnel wherein a nozzle is added to the downstream end of an expansion tube (refs. 3 and 4).

Another attack on the same problems is the use of simulation in which the test gas does not exactly duplicate all the flight conditions; instead, the test-gas parameters are so chosen as to duplicate the most important features of the flight system under study. A typical application of simulation to a different problem is the use of shock tubes to study the blunt-body stagnation-point heating rate of ballistic missiles (ref. 5). By correct duplication of the gas state at the stagnation point, the flow in a shock tube at a Mach number of 3 was employed to study experimentally a real-gas atmospheric reentry at hypersonic Mach numbers.

A study of the application of simulation to expansion tube operation was begun at Langley Research Center in 1961. Since the more recent atmospheric tables (ref. 6) and thermodynamic properties of air (ref. 7) were not available in 1961, the 1959 ARDC atmosphere (ref. 8) and air properties of references 9 and 10 form the basis for the analysis. Some of the results of this analysis together with a brief perfect-gas study of simulation in an expansion tunnel are presented in this report. A real-gas analysis of the expansion tunnel both with and without simulation is also under way at Langley but results are not sufficiently complete to be reported herein.

SYMBOLS

$\bar{A}$ area ratio of exit to inlet of nozzle in expansion tunnel

A_4 cross-section area of driver

a speed of sound

c_v specific heat at constant volume

E driver energy

H total enthalpy

h local enthalpy

l_D, l_{S_1}, l_{S_2} lengths of driver, intermediate (driven) chamber, and accelerating (expansion) chamber, respectively

M	Mach number
p	local pressure
p_0	standard atmospheric pressure
r	body nose radius
S/R	ratio of entropy S to gas constant R
s	local conditions at stagnation point of blunt body
T	local temperature
t	time
Δt_2	ideal test time (fig. 19)
U_{S_1}	primary shock velocity
u	fluid or flight velocity
Z	reciprocal molecular weight ratio, $\frac{\text{Undissociated molecular weight}}{\text{Dissociated molecular weight}}$
z	initial length of test-gas slug in intermediate chamber

$$\beta = \frac{\Gamma_1(M_e)}{\Gamma_1(M_f)}\left[\frac{\Gamma_2(M_f)}{\Gamma_2(M_e)}\right]^{1/2}$$

$$\Gamma_1(M_i) = 1 + \frac{\gamma - 1}{2} M_i$$

$$\Gamma_2(M_i) = 1 + \frac{\gamma - 1}{2} M_i^2$$

γ	ratio of specific heats
δ	normal-shock detachment distance
θ	flow-deflection angle

ϵ reciprocal of normal-shock density ratio, $\frac{\text{Density before shock wave}}{\text{Density after shock wave}}$

η_o ideal driver efficiency (eq. (28))

η_2, η_5 nondimensional time parameters, see reference 11

μ viscosity

ρ local density

σ shock-wave angle

Subscripts:

b local conditions behind normal shock

e entrance to expansion-tunnel nozzle

f exit from expansion-tunnel nozzle

i denotes gas in state i in cycle, identified by circled numbers in figure 1

∞ denotes gas in atmospheric flight (free stream)

$( )_i$ subscript signifies quantity to be evaluated in ith state

SIMULATION THEORY

Criteria for simulation are initially derived by matching the adiabatic-flow stagnation-point parameters behind a normal shock for a simulated free stream identified in figure 1 as region ⑤ to those of flight which are identified by the subscript ∞. (See following sketch.)

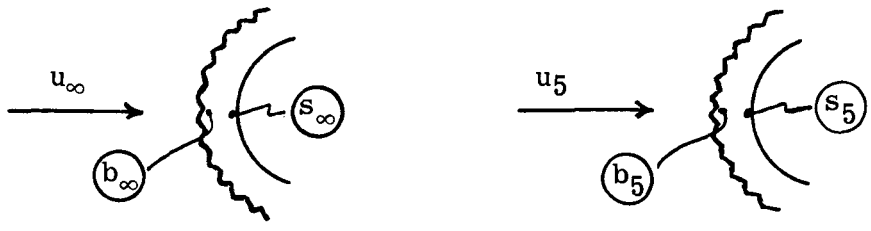

Flight Simulation

Since $H_5 = H_\infty$ at the stagnation point, conservation of energy requires that

$$\frac{u_\infty^2}{2} + h_\infty = \frac{u_5^2}{2} + h_5 \tag{1}$$

which may be manipulated to determine the simulation velocity ratio

$$\left(\frac{u_5}{u_\infty}\right)^2 = 1 + \frac{2h_\infty}{u_\infty^2}\left(1 - \frac{h_5}{h_\infty}\right) \tag{2}$$

Conservation of momentum across the shock wave is expressed as

$$p_\infty + \rho_\infty u_\infty^2 = p_{b_\infty} + \rho_{b_\infty} u_{b_\infty}^2 \tag{3}$$

Combining this equation and the continuity equation with the following incompressible Bernoulli equation

$$p_{b_\infty} + \frac{1}{2}\rho_b u_{b_\infty}^2 = p_{s_\infty} \tag{4}$$

which is assumed valid between the shock and stagnation point, yields the approximations for the stagnation pressure, as follows:

$$p_{s_\infty} \approx p_\infty + \rho_\infty u_\infty^2\left(1 - \frac{\epsilon_\infty}{2}\right) \tag{5}$$

$$p_{s_5} \approx p_5 + \rho_5 u_5^2\left(1 - \frac{\epsilon_5}{2}\right) \tag{5a}$$

Consequently, for equal stagnation pressures for both flight and simulation $\left(p_{s_\infty} = p_{s5}\right)$ the dynamic-pressure ratio is found from equation (5) to be

$$\frac{\rho_5 u_5^2}{\rho_\infty u_\infty^2} = \frac{1 - \frac{\epsilon_\infty}{2} + \frac{p_\infty}{\rho_\infty u_\infty^2}}{1 - \frac{\epsilon_5}{2} + \frac{p_5}{\rho_5 u_5^2}} \tag{6}$$

The simulation density ratio ρ_5/ρ_∞ results from combining equations (2) and (6)

$$\frac{\rho_5}{\rho_\infty} = \frac{1 - \frac{\epsilon_\infty}{2} + \frac{p_\infty}{\rho_\infty u_\infty^2}}{1 - \frac{\epsilon_5}{2} + \frac{p_5}{\rho_5 u_5^2}}\left[1 + \frac{2h_\infty}{u_\infty^2}\left(1 - \frac{h_5}{h_\infty}\right)\right]^{-1} \tag{7}$$

If the assumption of equilibrium and irreversible flow $\left(\frac{S_{b_5}}{R} \geqq \frac{S_5}{R}\right)$ is applied, the foregoing equations have a unique solution for any state ∞, since the following relationships exist:

For equilibrium composition,

$$p_5 = p_5(\rho_5, h_5) \tag{8}$$

For equal total enthalpies (eq. (2)),

$$u_5 = u_5(h_5) \tag{9}$$

For equilibrium normal shock,

$$\epsilon_5 = \epsilon_5(\rho_5, h_5, u_5) \tag{10}$$

$$= \epsilon_5(\rho_5, h_5) \tag{10a}$$

According to equation (7),

$$\rho_5 = \rho_5(\epsilon_5, p_5, h_5) \tag{11}$$

Thus, from equations (8), (10a), and (11),

$$\rho_5 = \rho_5(h_5) \tag{11a}$$

For a dissociating and ionizing gas, however, the solution is iterative rather than in closed form. Consequently, the sections to follow discuss the easily obtained but approximate solutions which are sufficiently accurate for the high velocities (Mach numbers) of interest.

PERFECT-GAS SIMULATION FOR EXPANSION TUBE AND EXPANSION TUNNEL

Since the purpose in illustrating the perfect-gas simulation is to indicate general performance trends at moderate values of T_5/T_∞, the hypersonic restriction of $M_\infty \gg 1$ and $M_5 \gg 1$ is introduced. Thus, equations (2) and (7) reduce to

$$\frac{u_5}{u_\infty} = 1 \tag{12}$$

$$\frac{\rho_5}{\rho_\infty} = 1 \tag{13}$$

The other simulation conditions are then

$$\frac{p_5}{p_\infty} = \frac{T_5}{T_\infty} \tag{14}$$

$$\frac{M_5}{M_\infty} = \frac{a_\infty}{a_5} = \sqrt{\frac{T_\infty}{T_5}} \tag{15}$$

Consequently the prediction of the performance of an expansion tube or tunnel simulating the conditions M_∞, p_∞ is simply reduced to the computation of a tube or tunnel with $M_5 = M_\infty\sqrt{\frac{T_\infty}{T_5}}$ and $p_5 = p_\infty\left(\frac{T_5}{T_\infty}\right)$. In particular, consider the ratio of the driver pressure to static pressure p_4/p_∞. The governing equation is equation (36) of reference 3 which is rewritten as

$$\frac{p_4}{p_5} = \left[1 - \frac{\gamma_4 - 1}{2} M_2 \frac{a_5}{a_4} \beta(M_5,\bar{A}) \frac{\Gamma_1(M_5)}{\Gamma_1(M_2)}\right]^{-\frac{2\gamma_4}{\gamma_4 - 1}} \left[\frac{\Gamma_1(M_5)}{\Gamma_1(M_2)} \beta(M_5,\bar{A})\right]^{\frac{2\gamma}{\gamma-1}} \tag{16}$$

Figure 1 of the present report gives the notation used for the expansion-tube cycle, and figure 1 of reference 3 gives that for an expansion tunnel. (Note that test state f of ref. 3 is replaced herein by state 5.) The driver-pressure ratio is then

$$\frac{p_4}{p_\infty} = \left(\frac{T_5}{T_\infty}\right)\left[1 - \frac{\gamma_4 - 1}{2} M_2 \frac{a_5}{a_4} \beta(M_5,\bar{A}) \frac{\Gamma_1(M_5)}{\Gamma_1(M_2)}\right]^{-\frac{2\gamma_4}{\gamma_4 - 1}} \left[\frac{\Gamma_1(M_5)}{\Gamma_1(M_2)} \beta(M_5,\bar{A})\right]^{\frac{2\gamma}{\gamma-1}} \tag{17}$$

In figure 2 curves are drawn of the ratio $(p_4/p_\infty)_{T_5 \neq T_\infty}$ to $(p_4/p_\infty)_{T_5 = T_\infty}$ by using equation (17) with $\gamma_4 = 5/3$, $\gamma = 1.4$, $\frac{a_\infty}{a_4} = \frac{49}{144}\sqrt{\frac{T_\infty}{T_4}}$ when $T_4/T_\infty = 10$ or 25 and $T_5/T_\infty = 1/3$, $10/3$, or $20/3$. This figure is the perfect-gas analogy to a heated helium-driven facility using driver temperatures T_4 of 3000° K and 7500° K with test-section air temperatures T_5 of 100° K, 1000° K, and 2000° K to simulate flight in an atmosphere where $T_\infty = 300^\circ$ K.

An approximate equation relating p_4/p_∞ to M_∞, T_5/T_∞, and $\bar{A}$ for $M_5 >> 1$ and $M_\infty >> 1$ is obtained by using equation (17b) of reference 3 for $\beta\Gamma_1(M_5)$:

$$\frac{p_4}{p_\infty} \approx \left(\frac{T_\infty}{T_5}\right)^{\frac{1}{\gamma-1}} \frac{\left[\frac{\gamma - 1}{2} M_\infty + \bar{A}^{\frac{\gamma-1}{2}} \sqrt{\frac{T_5}{T_\infty}}\right]^{\frac{2\gamma}{\gamma-1}} \left[\Gamma_1(M_2)\right]^{-\frac{2\gamma}{\gamma-1}}}{\left[1 - \frac{\gamma_4 - 1}{2} \frac{(M_2)}{\Gamma_1(M_2)} \frac{a_\infty}{a_4}\left(\frac{\gamma - 1}{2} M_\infty + \bar{A}^{\frac{\gamma-1}{2}} \sqrt{\frac{T_5}{T_\infty}}\right)\right]^{\frac{2\gamma_4}{\gamma_4 - 1}}} \tag{18}$$

The variation of the ratio of the driver pressure $(p_4)_{T_5 \neq T_\infty}$ to $(p_4)_{T_5=T_\infty}$ over a wide range on both sides of unity may be understood by consideration of the terms in equation (18). For small values of $\overline{A}$ the term $\left(\frac{T_\infty}{T_5}\right)^{\frac{1}{\gamma-1}}$ dominates in the lower range of M_∞ and the driver-pressure requirements are reduced by a simulation in which $T_5 > T_\infty$. As M_∞ increases the relative contribution of the temperature-ratio term is reduced, and the driver-pressure ratio decreases further. However, as M_∞ increases still further, the bracketed denominator becomes smaller so that the driver-pressure ratio begins to rise. (Note that there is a limiting M_∞ when the pressure ratio p_4/p_∞ becomes infinite.)

As $\overline{A}$ increases with other conditions fixed, the driver-pressure ratio increases because the numerator of the fraction (eq. (18)) increases while the denominator decreases; and this pressure increase is further undesirably augmented by simulation when $T_5 > T_\infty$. Thus, in regard to the driver-pressure requirements there is a restricted range where the use of simulation with $T_5 > T_\infty$ is advantageous. When $T_5 < T_\infty$ the ratio of $(p_4)_{T_5 \neq T_\infty}$ to $(p_4)_{T_5=T_\infty}$ is greater than unity for $10 < M_\infty < 50$ and $1 \leqq \overline{A} \leqq 10^3$ (fig. 2(a)). Consequently, on a driver-pressure basis, simulation with $T_5 > T_\infty$ appears more advantageous in this Mach number and area range.

Equilibrium-air calculations for simulation with $\overline{A} > 1$ have been under way for some time at Langley Research Center, but are not considered in this analysis. The next section treats the particular case of $T_5 > T_\infty$ and $\overline{A} = 1$ for the expansion tube.

EQUILIBRIUM AIR SIMULATION FOR EXPANSION TUBE

Conditions in Various States of Cycle

Conditions in test-gas region 5.- To simplify the determination of u_5/u_∞ and ρ_5/ρ_∞ for equilibrium real air, the following approximate scheme is used. First, the right-hand side of equation (6) is assumed to be unity. Such an assumption introduces only a small error for large u_∞ since $\epsilon_\infty \approx \epsilon_5 \ll 1$ and $\frac{p}{\rho u^2} \approx \frac{1}{\gamma M^2} \ll 1$. Second, in equations (1), (2), or (7) the term $2h_\infty/u_\infty^2$ was assumed to be negligible compared to unity $\left(\text{i.e., } M_\infty^2 \gg \frac{2}{\gamma - 1}\right)$; but the term $2h_5/u_\infty^2$ was retained so as to increase the accuracy of the solutions since M_5^2 is of the order of $\frac{T_\infty}{T_5} M_\infty^2$. Because the independent parameters selected were ρ_∞, h_∞, u_∞, and T_5 (rather than h_5), the retention of the h_5 term required an iterative solution which, however, converged very rapidly so that acceptable accuracy was obtained after a single iteration to the following modified equations:

$$\left(\frac{u_5}{u_\infty}\right)^2 \approx 1 - \frac{2h_5}{u_\infty{}^2} \tag{19}$$

$$\frac{\rho_5}{\rho_\infty} \approx \left(\frac{u_\infty}{u_5}\right)^2 \tag{20}$$

$$h_5 = h_5(\rho_5, T_5) \tag{21}$$

$$p_5 = p_5(\rho_5, T_5) \tag{22}$$

Equations (19) to (22) were solved for the simulation state 5 when $T_5 = 1000^\circ$ K and 2000° K. The ambient conditions simulated were for velocities u_∞ between 20 000 and 50 000 feet per second (6.096 and 15.24 km/sec) at densities ρ_∞ and temperatures T_∞ corresponding to flight altitudes of 100 000, 150 000, 200 000, 250 000, and 300 000 feet. Since this calculation was performed prior to the release of the U.S. 1962 standard atmosphere (ref. 6), values of the ARDC 1959 model atmosphere (ref. 8) were employed for flight conditions ∞. The differences between the two atmospheres are significant only for the highest of the altitudes considered herein.

The normalized simulation conditions of the test region (state 5) appear in figures 3 to 7. The normalized velocity ratio u_5/u_∞ (fig. 3) has an increased departure from unity for lower velocities and increased T_5; this effect is a direct result of the retention of the $h_5/u_\infty{}^2$ term which increases as T_5 increases or $u_\infty{}^2$ decreases. For $T_5 = 1000^\circ$ K, $0.975 < \frac{u_5}{u_\infty} < 0.997$ and for $T_5 = 2000^\circ$ K, $0.922 < \frac{u_5}{u_\infty} < 0.991$ in the velocity range 20 000 to 50 000 feet per second (6.1 to 15.24 km/sec). The normalized density ratio (fig. 4) has twice the variation of the velocity ratio (eq. (20)) with a maximum value of 1.05 and 1.18 for $T_5 = 1000^\circ$ K and 2000° K, respectively, at the lowest velocity. The reciprocal molecular weight ratio Z_5 (fig. 5), which (because the Van der Waal forces are negligible in the test region 5) is equivalent to the compressibility factor, is essentially unity for $T_5 = 1000^\circ$ K. For $T_5 = 2000^\circ$ K, Z_5 varies with altitude from 1.00 up to 1.04. Note that figure 5 does not indicate a variation of Z_5 with u_∞ at a given altitude. Actually, there is a small variation with u_5, but except at the highest altitude, it is not discernible within the resolution of this figure, and hence an average value is plotted.

The fraction of the total enthalpy due to ambient dissociation is less than 1 percent for altitudes below 250 000 feet (76.2 km) and $T_5 = 2000^\circ$ K. However, at 300 000 feet (91.44 km) the dissociation energy for $T_5 = 2000^\circ$ K is 3 percent and 1 percent of the total enthalpy for $u_\infty = 20\,000$ and 50 000 ft/sec (6.096 and 15.24 km/sec), respectively. Such small percentages should not distort the resultant model flow fields significantly.

The normalized pressure ratio p_5/p_∞ (fig. 6) exhibits a larger variation with altitude for given velocity than either the density or velocity. This variation arises mainly because T_∞ is a function of altitude, but it is also influenced slightly by Z_5 (for $T_5 = 2000^\circ$ K). Consequently, since $\frac{p_5}{p_\infty} = Z_5 \frac{T_5}{T_\infty} \frac{\rho_5}{\rho_\infty}$, the variation of p_5/p_∞ with altitude will be larger than that of ρ_5/ρ_∞.

The normalized viscosity ratio μ_5/μ_∞ (fig. 7) is also dependent on altitude. Since the Reynolds number ratio $\frac{\rho_5 u_5}{\mu_5} \frac{\mu_\infty}{\rho_\infty u_\infty} = \frac{u_\infty}{u_5} \frac{\mu_\infty}{\mu_5}$, the viscosity ratio essentially determines the Reynolds number ratio. Figure 7 thus indicates a lowering of the Reynolds number by factors up to 6, which occur in simulation at 2000° K. Since wave attenuation, boundary-layer growth, and test-gas velocity profile are all influenced by Reynolds number, this lower Reynolds number is an undesirable feature of simulation. (See ref. 3.)

The dimensionless entropy S_5/R is plotted in figure 8 as a function of altitude. Although only a single line is shown for both $T_5 = T_\infty$ and $T_5 = 1000^\circ$ K, the calculations for $T_5 = 1000^\circ$ K actually plot a family of curves, which are not separable within the definition of the figure. The two extremes of this family are shown for $T_5 = 2000^\circ$ K; the difference in S_5/R between $u_\infty = 20\,000$ ft/sec (6.096 km/sec) and $u_\infty = 50\,000$ ft/sec (15.24 km/sec) is very small.

Conditions for region 2.- The conditions for region 2 were determined from those in region 5 by using the charts of reference 11 for equilibrium one-dimensional unsteady isentropic flows, together with the values of u_5 and S_5/R from figures 3 and 8. In certain cases a slight extrapolation of the data in references 9 and 10 was necessary to obtain the conditions in region 2 but the errors so introduced are believed small. No computations were completed for $u > 35\,000$ ft/sec (10.668 km/sec) at an altitude of 100 000 feet (30.48 km) because the required extrapolations became too large. Since these computations were completed, reference 7 has been published and the data therein would eliminate the necessity for such extrapolation.

Figure 9 shows that the flow velocity u_2 increases as T_5 increases for a given u_∞. This trend is to be expected since the total enthalpy multiplication ratio H_5/H_2 is reduced by expanding only to M_5 instead of M_∞. (See eq. (16) and fig. 7 of reference 1.) Note, however, that M_5 of this reference is equivalent to the M_5 herein only for $T_5 = T_\infty$. Consequently, since $H_2 \approx u_2^2$, a higher value of u_2 is required to produce the same H_5.

Temperatures T_2 for simulation are also generally increased for $T_5 = 1000^\circ$ K and 2000° K (fig. 10). The explanation of this variation follows along the same lines as that in the previous paragraph since $H_2 \approx 2h_2$, and in general for small dissociation T_2

varies as h_2. However, for appreciable dissociation the temperature is depressed. This depression is responsible for the approximate invariance in T_2 with T_5 at the higher velocities.

In contrast to both the temperature and velocities in region 2 and pressures in region 5, the pressures for simulation in region 2 with $T_5 > T_\infty$ are lower for a given velocity and altitude. These pressures, normalized by standard atmospheric pressure p_0 in figure 11, are approximately a decade lower when $T_5 = 2000^\circ$ K than when $T_5 = T_\infty$. Thus, the increased simulation entropy more than compensates for the increased T_2 with the net result that p_2 decreases.

One of the principal disadvantages of simulation with $T_5 > T_\infty$ is evident from the data shown in figure 12; namely, the appreciable increase in Z_2 for $T_5 = 1000^\circ$ K or 2000° K. When $T_5 = T_\infty$, $Z_2 = 1.00$ at $u_\infty = 20\,000$ feet per second (6.096 km/sec), whereas when $T_5 = 2000^\circ$ K the values of Z_2 vary from 1.06 to 1.15. Similarly, at $u_\infty = 50\,000$ feet per second (15.24 km/sec), $1.09 \leq Z_2 \leq 1.18$ for $T_5 = T_\infty$, whereas $1.20 \leq Z_2 \leq 1.33$ for $T_5 = 2000^\circ$ K. Since by the definition of Z used herein, the mass fraction dissociated is essentially $Z - 1$, the dissociation in region 2 has been approximately doubled in a change from $T_5 = T_\infty$ to $T_5 = 2000^\circ$ K at $u_\infty = 50\,000$ feet per second (15.24 km/sec). If these atoms are not recombined (i.e., if flow "freezes") during or following the unsteady expansion, then a larger degree of dissociation will exist at the test section than is indicated in figure 4. The fact that Z_2 is higher and ρ_2 is lower for simulation than for duplication increases the possibility of a greater degree of nonequilibrium or even of a frozen test gas for simulated testing as compared with that for duplication. Countering these adverse factors and tending to maintain equilibrium for simulation is the much slower rate of expansion which the test gas experiences because the test time is longer and the last part of the test-gas slug therefore enters the unsteady centered expansion wave farther from the singularity at the origin. The test time and slug length are discussed in a subsequent section of this paper. Of course, even the values of Z_2 at 2000° K are much less than the maximum Z occurring before the nozzle expansion in a reflected shock tunnel. For example, at $u_\infty = 30\,000$ feet per second (9.144 km/sec) and an altitude of 200 000 feet (60.96 km) a reflected shock tunnel would require a Z at the nozzle entrance of approximately 1.35 as contrasted to $Z_2 \approx 1.16$ for $T_5 = 2000^\circ$ K. Thus for $u_\infty = 30\,000$ feet per second (9.144 km/sec) at 200 000 feet (60.96 km) altitude the shock-tunnel dissociation would still be about twice the expansion-tube value with 2000° K simulation.

Conditions for region 1.- The shock velocity U_{S_1} and pressure p_1 were determined from the charts of reference 11 for $T_1 = 300^\circ$ K. The trend of U_{S_1} for simulation (fig. 13) is, as expected, similar to that of u_2 (fig. 9) with U_{S_1} increasing as T_5 increases. Also, p_1/p_0 (fig. 14) decreases in approximately the same manner as

p_2/p_0 (fig. 11). The fact that lower values of p_1/p_0 are required means an increased vacuum capability for the intermediate chamber with minimum pressures of p_1/p_0 of the order of 10^{-5} for $T_5 = 2000^\circ$ K as compared with values on the order of 10^{-3} for $T_5 = T_\infty$ (fig. 14). However, such values of p_1/p_0 are fairly easily obtained and are significantly above the values of p_{10}/p_0 (which are the minimum pressures in the overall apparatus) to be discussed in the following paragraph.

Conditions for region 10.- Perfect helium was arbitrarily assumed for both regions 20 and 10, and the approximation of a strong shock was invoked. Consequently, equation (3) of reference 1 was used to obtain p_{20}/p_{10}; and p_{10}/p_0 then follows since $p_{20} = p_5 = \left(\frac{p_5}{p_\infty}\right)p_\infty$. In this case, values of $T_5 > T_\infty$ are beneficial because p_{10}/p_0 increases as T_5 increases (fig. 15) and reduces the vacuum requirements of the expansion chamber. This increased pressure is a substantial advantage since the difficulty in obtaining $p_{10}/p_0 = 3 \times 10^{-8}$ is much less than in obtaining $p_{10}/p_0 = 2 \times 10^{-9}$. (These values are for $T_5 = 2000^\circ$ K and $T_5 = T_\infty$, respectively, at $u_\infty = 50\,000$ feet per second (15.24 km/sec) for an altitude of 300 000 feet (91.44 km). The assumptions of perfect helium and a strong shock are naturally questionable at these low pressures.

Conditions for driver region 4.- Three driver gases are considered to illustrate conditions in the driver region 4:

(1) A combustion driver consisting of a mixture of 75 percent helium with 25 percent of a stoichiometric mixture of oxygen and hydrogen (fig. 16);

(2) Hydrogen heated to $T_4 = 833^\circ$ K (fig. 17);

(3) Helium heated to $T_4 = 4000^\circ$ K (fig. 18)

These drivers might be considered typical of those heated, respectively, by combustion (ref. 12), electric resistance heaters (either external or internal, refs. 13 and 14), and electric-arc heating to moderate T_4. Appreciable reductions in driver-pressure ratio p_4/p_0 result from simulation with a decrease of approximately a decade apparent for the three driver gases. The driver pressures required for given T_5, u_∞, and altitude are nearly equal for the combustion and hydrogen drivers (figs. 16 and 17), whereas pressures for the heated helium are somewhat lower (fig. 18).

Lengths of Component Sections

A wave diagram of the component sections in the expansion tube is illustrated in figure 19. The ratio of the intermediate chamber length l_{S_1} to the accelerating chamber length l_{S_2} is chosen so that the reflected wave originating from the intersection of the upstream edge of the expansion fan with the entropy discontinuity (point III of fig. 19) arrives at the test section concurrently with the downstream edge of the expansion

fan (point II). From this wave diagram the time interval between the secondary diaphragm rupture and point III may be simply related to the length l_{S_1}, the conditions in region 2, and the primary shock speed. Similarly, the time interval to point II is $\frac{l_{S_2}}{u_5 - a_5}$. Since these time intervals may also be expressed as $f(\eta)$ (see eq. (15) of ref. 11), it follows that the ratio of l_{S_1} to l_{S_2} may be expressed as

$$\frac{l_{S_1}}{l_{S_2}} = \frac{U_{S_1}}{u_5 - a_5} \frac{a_2}{U_{S_1} - u_2} \left[\frac{a_5}{a_2} \exp(\eta_5 - \eta_2)\right]^{1/2} \tag{23}$$

Charts of η from reference 11 were used to evaluate equation (23) and the resulting ratios l_{S_1}/l_{S_2} are shown in figure 20. Increased intermediate chamber length ratio l_{S_1}/l_{S_2} is required for $T_5 > T_\infty$ with nearly a decade increase required for $T_5 = 2000^\circ$ K over values for $T_5 = T_\infty$. However, this increase is not of major concern for practical designs except at the lower velocities; for example, for $T_5 = 2000^\circ$ K, $l_{S_1}/l_{S_2} \approx 0.3$ at $u_\infty = 20\,000$ feet per second (6.096 km/sec) and $l_{S_1}/l_{S_2} \approx 0.02$ at $u_\infty = 50\,000$ feet per second (15.24 km/sec).

The values of l_{S_1}/l_{S_2} of figure 20 for $T_5 = T_\infty$ are not identical with those of reference 15 (fig. 11) or with the ratios obtained from figures 14 and 15 of reference 1 because of the approximate integration scheme used in those references. However, the variation is small except for one case where an error in integration resulted in an incorrect value in references 1 and 15 for l_{S_1} at an altitude of 250 000 feet (76.2 km).

The driver chamber length l_D was chosen to match the intermediate chamber length l_{S_1} so that the initial reflection from the end of the driver would pass through point III, figure 19. The governing equation, which follows, was derived by equating the time necessary for the entropy discontinuity to travel the distance $x_{III} = \frac{t_{III}}{u_2}$ to the sum of the times required for the reflected wave to: (a) traverse the driver in a negative direction, (b) traverse the driver expansion fan, and (c) traverse region 3 to point III.

$$\frac{l_D}{l_{S_1}} = \left(1 + \frac{U_{S_1} - u_2}{a_2}\right) \frac{a_4}{2U_{S_1}} \left(\frac{a_3}{a_4}\right)^{\frac{\gamma_4 + 1}{2(\gamma_4 - 1)}} \tag{24}$$

The sound speed ratio for the driver expansion is

$$\frac{a_3}{a_4} = 1 - \frac{\gamma_4 - 1}{2} \frac{u_2}{a_4} \tag{25}$$

The length ratios l_D/l_{S_1} are shown in figures 21 to 23 for the three driver gases of figures 16 to 18. In all cases the ratio l_D/l_{S_1} decreases as T_5 increases. At $T_5 = 2000^\circ$ K the driver length ratio l_D/l_{S_1} is approximately one-half that required for $T_5 = T_\infty$. However, this decrease in l_D/l_{S_1} is not sufficient to offset the increase in l_{S_1}/l_{S_2}, with the net result that the ratio l_D/l_{S_2} is an order of magnitude larger for $T_5 = 2000^\circ$ K than for $T_5 = T_\infty$. The significance of the ratio l_D/l_{S_2} is discussed further in a subsequent section.

Test Time Per Unit Length

One of the most critical factors in expansion-tube operation is the length of the ideal test time, which is indicated as Δt_2 (fig. 19). The ideal test time per unit accelerating chamber length $\Delta t_2/l_{S_2}$ is plotted in figure 24. Significant gains are realizable for increasing T_5; at $T_5 = 2000^\circ$ K, $\Delta t/l_{S_2}$ is roughly larger by a factor of 3 than that for $T_5 = T_\infty$ at the same u_∞ and altitude. In a practical application, gains larger than those just mentioned may be possible since the actual test time will be less than the ideal time by the time required to establish the flow about a model once the fluid in state 5 reaches the model, as well as by the time lost due to mixing and other effects. These flow-establishment and mixing-loss times should not change appreciably with simulation. Thus, consider a case where the actual test time was only 25 percent of the ideal test time when $T_5 = T_\infty$. Then, for the same lost time and an ideal test time with simulation larger by a factor of 3, the actual simulation test time would be 900 percent of that for $T_5 = T_\infty$.

Although simulation increases $\Delta t_2/l_{S_2}$, the opposite trend results for $\Delta t_2/l_{S_1}$ (fig. 25). Consequently for given flight conditions ∞ and ideal test time, a longer intermediate chamber is required. The values of $\Delta t/l_{S_1}$ for $T_5 = T_\infty$ are roughly 5 to 7 times larger than those for $T_5 = 2000^\circ$ K.

Initial Test Slug Length

The criticalness of the secondary diaphragm rupture because of the very limited axial distance occupied by the test-gas slug while in regions 1 and 2 has been pointed out in references 1, 3, and 4. The quantity z is defined as the initial extent of the test gas slug in region 1; that is,

$$z \equiv \frac{\rho_5}{\rho_1} \frac{A_5}{A_1} u_5 \Delta t \tag{26}$$

where for purposes of this analysis $\Delta t = \Delta t_2$ in equation (26). The normalized ratio z/l_{S_2} exhibits very large gains for simulation with $T_5 > T_\infty$ (fig. 26). In fact, for $T_5 = 2000^\circ$ K, z/l_{S_2} is approximately two orders of magnitude greater than that for

$T_5 = T_\infty$. Of course, even with such gains, the absolute value of z/l_{S_2} is still very small at the higher velocities. The possibility of further increasing z/l_{S_2} by a combination of simulation with expansion tunnel operation is a fruitful field for investigation since both modes of operation individually increase z/l_{S_2} significantly.

Driver Considerations

Arc driver energy.- Although for the combustion or resistance heated driver gases the states in region 4 available to the experimenter are primarily determined by p_4, which is in turn limited by the strength of the driver vessel, the user of an electric-arc discharge-heated driver gas is additionally limited by the amount of energy E in his condenser bank or inductive field (assuming 100 percent arc efficiency). A convenient parameter to evaluate this energy restriction is the driver energy density $E/A_4 l_D$, which for a perfect driver gas is

$$\frac{E}{A_4 l_D} = (\rho c_v T)_4 \left(1 - \frac{T_i}{T_4}\right) \tag{27}$$

Since the driver energy density for a perfect gas is simply related to the driver pressure p_4, the variation in energy density of figure 27 for a helium driver at $T_4 = 4000^\circ$ K follows the pressure variation of figure 18. Again for otherwise comparable conditions a decrease in $E/A_4 l_D$ of approximately a decade occurs between $T_5 = T_\infty$ and $T_5 = 2000^\circ$ K. This energy parameter will vary with T_4. (See, for example, the variation of p_4 with T_4 in fig. 12(a) of ref. 1.) Even with simulation, large values of E are required for expansion tubes of practical size since for $T_5 = 2000^\circ$ K, $u_\infty = 50\,000$ ft/sec (15.24 km), $\frac{E}{A_4 l_D} \approx 3 \times 10^4$ joules/ft^3 $\left(1 \times 10^6 \text{ joules/m}^3\right)$ at 300 000 feet (91.44 km) altitude and 1×10^8 joules/ft^3 $\left(4 \times 10^9 \text{ joules/m}^3\right)$ at 100 000 feet (30.48 km).

Although the energy density parameter permits the matching of the energy source E with the driver dimensions, this parameter gives no indication of the gains or losses from simulation, since the driver length l_D required also varies with the degree of simulation. However, such an indicative parameter is the ideal driver efficiency η_o, which is the ratio of the kinetic energy of the test-section gas to the driver energy E:

$$\eta_o \equiv \frac{\left(\frac{1}{2} u_5^2\right)\left(\rho_5 u_5 \Delta t_2 A_5\right)}{E} \tag{28}$$

From figure 28 it is evident that simulation does improve the ideal efficiency with typical increases of half a decade at the higher velocities. Caution should be exercised in the use of this figure because of the inherent assumption that the lengths l_D and l_{S_1} can be continuously varied to obtain the previously discussed optimum ratios of

l_D/l_{S_1} and l_{S_1}/l_{S_2}. However, even with the moderate flexibility obtainable by the use of a number of finite sections to comprise the various chambers, most of the gains due to an infinite flexibility should be attainable since configurations both with and without simulation would be penalized.

Another factor to be weighed is the ideal length of the driver required as compared with the practical physical size from consideration of viscous effects, diaphragm rupture, and other factors. For example, the ratio l_D/l_{S_2} formed from figures 20 and 23 is plotted in figure 29. Note that larger values of l_D/l_{S_2} are required for simulation; for example, at 50 000 feet per second (15.24 km/sec) $\frac{l_D}{l_{S_2}} \approx 1.5 \times 10^{-4}$ at $T_5 = T_\infty$ and $\frac{l_D}{l_{S_2}} \approx 2 \times 10^{-3}$ at $T_5 = 2000^\circ$ K. Assuming a value of $l_{S_2} = 100$ feet (30 m) and a diameter of 1 foot (0.3 m), then the ideal $l_D \approx 0.015$ foot (0.005 m) for $T_5 = T_\infty$ and 0.2 foot (0.06 m) for $T_5 = 2000^\circ$ K. Such lengths appear unrealistic for a 1-foot-diameter driver; in fact, a driver length-to-diameter ratio of unity might be a practical minimum. In such a case the ideal efficiencies of figure 27 would be reduced by factors of 0.015 and 0.2, respectively, so that the half-decade ideal efficiency gains for simulation become "practical efficiency" gains of a decade and a half.

Typical maximum-velocity-performance comparison.- The maximum u_∞ performance of an expansion tube with and without simulation was determined from figures 16 and 17 for combustion (75 percent He) and hydrogen $(T_4 = 833^\circ$ K) driver with a maximum $p_4 = 20\,000$ psi $(1.36 \times 10^3$ atm) and also from figure 27 for a helium driver $(T_4 = 4000^\circ$ K) with $E = 2.5 \times 10^6$ joules, $A_4 = 1$ ft^2 $(0.09$ m$^2)$, $l_D = 1$ ft (0.3 m). Note that these three drivers give almost identical performance for $T_5 = T_\infty$ (fig. 30). However, as T_5 increases the gains in u_∞ are smaller for the combustion and hydrogen drivers than for the helium driver. For $T_5 = 2000^\circ$ K a general rule of thumb describing the simulation gains for all three drivers might be an increase in u_∞ of roughly 10 000 feet per second (3.048 km/sec) at the same altitude, or reduction in altitude of 75 000 feet (22.86 km) at the same u_∞. Such performance increases are very significant gains in facility capability.

EFFECT OF SIMULATION ON FLOW FIELDS

Equilibrium Case

The simulation method investigated was selected to duplicate equilibrium conditions at the stagnation point of a blunt body in hypersonic flow. Since the gas states do not change appreciably in the stagnation region bounded by the normal shock and the blunt-body stagnation point, the conditions behind the normal shock should also be closely duplicated. For a given body nose radius r, the shock detachment distance δ is inversely proportional to the stagnation-region density ratio; consequently, the ratio

$\frac{(\delta/\dot{r})_5}{(\delta/r)_\infty}$ will be proportional to the ratio ρ_5/ρ_∞. The data of figure 4 imply that the ratio δ_5/δ_∞ at $T_5 = 1000^\circ$ K decreases from 1.05 at $u_\infty = 20\,000$ ft/sec (6.096 km/sec) to 1.01 at $u_\infty = 50\,000$ ft/sec (15.240 km/sec). At $T_5 = 2000^\circ$ K the discrepancy is increased, with a variation in δ_5/δ_∞ from approximately 1.15 at $u_\infty = 20\,000$ ft/sec to 1.02 at $u_\infty = 50\,000$ ft/sec. If the maximum deviation acceptable was 10 percent, then simulation at $T_5 = 2000^\circ$ K would be valid only for $u_\infty > 25\,000$ ft/sec (7.620 km/sec).

Simulation decreases the test section Mach number M_5 approximately as the square root of T_∞/T_5 (fig. 31). Such a drastic reduction in Mach number might be important if the reduced Mach number was not still hypersonic and if the test fluid did not satisfy the simulation requirements herein. However, even for the lowest velocity considered in this paper, the Mach number is above 7 ($u_\infty = 20\,000$ ft/sec (6.096 km/sec), $T_5 = 2000^\circ$ K). References 16 and 17 indicate that for strong shock waves in a real gas the total enthalpy is the most important parameter influencing shock shape and total enthalpy is conserved in simulation.

Shock-wave polars for the simulated flows were computed by the equilibrium normal-shock program of reference 18. The results are shown in figures 32 to 35 where the left- and right-hand ordinates refer to $u_\infty = 20\,000$ and 50 000 ft/sec (6.096 and 15.240 km/sec), respectively. At $u_\infty = 50\,000$ ft/sec the correspondence in shock-wave angles (σ) for a given flow deflection across the shock wave (θ) continues to be excellent down to very low values of σ and θ (fig. 32). For $u_\infty = 20\,000$ ft/sec (6.096 km/sec) this correspondence is not quite so good but is still very satisfactory from the normal shock case down to weak shock deflections approaching 20°; for lower θ's the deviations must increase since at $\theta = 0$ the shock angle becomes the Mach angle which varies in accord with the Mach number of figure 31.

The density behind the shock wave normalized by the ambient flight density is plotted in figure 33. When $u_\infty = 50\,000$ ft/sec (15.240 km/sec), the curves for $T_5 = 1000^\circ$ K and 2000° K follow the curve for $T_5 = T_\infty$ within 5 percent from normal shock to weak shocks where $\theta \approx 20^\circ$. As expected the variation is greater when $u_\infty = 20\,000$ ft/sec (6.096 km/sec), but even here the correspondence is good down to the point where oxygen dissociation is essentially complete as indicated by the "bump" on the curves at $\theta \approx 35^\circ$ for 200 000 feet (60.96 km) and $\theta \approx 30^\circ$ at 300 000 feet (91.44 km). After passing across the "bump" the correspondence improves again down to $\theta \approx 20^\circ$ where another divergence occurs.

The post shock temperature (fig. 34) also shows only minor deviations with T_5 down to flow deflections of 20° for $u_\infty = 50\,000$ ft/sec (15.240 km/sec). The deviation is, as expected, greater for $u_\infty = 20\,000$ ft/sec (6.096 km/sec) and although it is

roughly 500° K for $\theta = 20^{\circ}$ a wider discrepancy appears for $30^{\circ} < \theta < 40^{\circ}$ where the aforementioned dissociation effect is apparent.

The post shock reciprocal molecular weight ratio is the last shock wave parameter illustrated (fig. 35). As in the preceding two figures the correspondence is best at the higher velocity and lower altitude. Note the effect of the ambient dissociation $Z_5 - 1$ (fig. 5) which causes the divergence of the weak shock curves as θ becomes small.

Reference 19 considered the effects of a constant total enthalpy simulation fairly similar to that of the present report. Attention was directed toward larger values of Z so that in the approximate energy equation used therein, the thermal energy was negligible as compared with the dissociation energy (i.e., h_5 in eq. (19) was replaced by the dissociation energy) and furthermore a hypersonic approximation was invoked requiring the kinetic energy normal to a shock wave to be much larger than the ambient thermal energy. Nevertheless, the results of reference 19 should still provide some guidelines for the present analysis. The symbol α_{∞_2} of reference 19 is equivalent to $Z_5 - 1$ herein. Since $Z_5 - 1$ is less than 0.04 for equilibrium expansion to region 5, figures 13 to 19 of reference 19 show that the effect of predissociation is insignificant for the normal-shock condition but is more significant for an attached shock with flow deflection of 30°. For this latter condition the hypersonic approximation used in reference 19 is not on firm ground. Flow-detachment angle and flow deflection at attachment are also little changed at $Z = 1.04$.

Thus, in regard to simulation under equilibrium conditions one would expect fairly good reproduction of the body flow fields with less departure at the higher velocities and stronger shock waves associated with blunter bodies.

Nonequilibrium Case

Although the energy in vibration or dissociation in the test gas is small compared with the flow kinetic energy when the test gas in region 5 is assumed in equilibrium, the mere existence of these higher energy levels in the test stream as well as the presence of atomic oxygen can appreciably influence the gas chemistry. In reference 20, theoretical calculations were made at ambient conditions of $T = 294^{\circ}$ K, $\rho = 3.15 \times 10^{-8}$ grams/cm^3, and $Z = 1.0$ and 1.1 for shock speeds of 5.9 and 7.2 mm/μsec ($u_{\infty} = 19\,000$ and 24 000 ft/sec). These calculations showed that for the predissociated free-stream case the oxygen, nitric oxide, nitrogen, and electron concentrations as well as radiation from the N_2^+ and NO^* systems were initially increased at the same position after the shock when compared with the undissociated free-stream case. However, the maximum and equilibrium concentrations were not greatly different, although the positions of maximum overshoot and maximum nonequilibrium radiation were closer to the shock wave. For a slower shock speed of 4.1 mm/μsec ($u_{\infty} = 13\,000$ ft/sec)

the deviations were more pronounced, especially in regard to the radiation where the overshoot was significantly higher when $Z = 1.1$.

Although the condition of nonunity in ambient Z was considered in reference 20, the case of concurrently varying ambient temperature and velocity was not examined. A brief treatment of the latter case may be found in reference 19. No further discussion of the finite chemistry and associated nonequilibrium radiation is contained herein since generalizations other than the following statements are difficult: (a) The initial ambient dissociated oxygen should increase the concentrations closely behind the shock wave of oxygen as well as nitrogen and nitric oxide, which require molecular oxygen as an intermediate product; (b) if the model size is so small that equilibrium is not reached in the stagnation region, then the influence of the oxygen atoms in the test section permeate the entire flow field; and (c) the deviations will become more significant as the shock wave becomes less normal.

RÉSUMÉ

This analysis has considered the effects of simulation wherein blunt-body stagnation conditions were closely matched for simulated and flight conditions. The simulation mode selected was variation of the temperature of the test medium T_5 in the expansion tunnel or expansion tube.

A brief perfect-gas treatment of expansion-tunnel operation with simulation showed that both increases and decreases in driver gas pressure p_4 resulted, depending on the tunnel area ratio $\overline{A}$, driver temperature ratio T_4/T_∞, simulation temperature ratio T_5/T_∞, and flight Mach number M_∞. The use of simulation when T_5/T_∞ was less than unity did not appear advantageous from driver-pressure requirements for $20 < M_\infty < 50$ and $1 < \overline{A} < 10^3$.

A more thorough equilibrium real-air study of expansion-tube operation comparing simulation at $T_5 = 1000^\circ$ K and 2000° K with exact duplication when $T_5 = T_\infty$ showed the following:

Principal Advantages of Simulation:

1. The ideal testing time per unit expansion chamber length $\left(\Delta t_2 / l_{S_2}\right)$ increases significantly.

2. The ratio of initial test gas slug length to the expansion-chamber length $\left(z / l_{S_2}\right)$ increases by orders of magnitude.

3. Equilibrium flow fields and radiation should be similar for the same body shape with similarity increasing with increases in velocity and body bluntness.

4. Driver-pressure requirements are markedly reduced; or conversely, the performance potential in terms of flight velocity and altitude for a given driver are greatly increased.

5. The efficiency of an arc-heated helium driver is increased.

6. The minimum pressure required in the expansion chamber is increased an order of magnitude and thus vacuum pumping requirements are reduced.

Principal Disadvantages of Simulation:

1. The reciprocal test-section molecular weight ratio Z_5 departs from unity for $T_5 = 2000^{\circ}$ K. The resulting degree of dissociation $(Z_5 - 1)$ can contribute up to 3 percent of the total enthalpy (H_5) for the worst case evaluated, namely, flight velocity $u_\infty = 20\,000$ ft/sec (6.1 km/sec), altitude = 300 000 ft (91.44 km).

2. The higher initial thermal and (for $Z_5 \neq 1$) chemical energy of the test-section gas for $T_5 = 1000^{\circ}$ K and 2000° K may significantly influence finite rate chemistry. Consequently, nonequilibrium flow fields and radiation may vary with simulation; the variation will probably be greater for lower velocities, lower shock wave angles, lower densities, and smaller models.

3. The degree of dissociation behind the primary shock wave $(Z_2 - 1)$ increases significantly with simulation. If freezing does not occur in the unsteady expansion, then large Z_2 is not important. However, if appreciable freezing occurs, then Z_5 would be increased above the equilibrium values.

4. Larger lengths of intermediate chamber (l_{S_1}) and driver chamber (l_D) are required for a given l_{S_2}. However, for high values of u_∞ where the advantages of simulation become marked, the lengths l_D and l_{S_1} are still approximately two orders of magnitude less than l_{S_2}.

5. The test-section Mach number is reduced, but this reduction is not a significant penalty as long as flow is still hypersonic.

6. The test-section viscosity is increased. The detrimental extent of this effect on test core size and attenuation is not known.

The relative significance of the aforementioned advantages and disadvantages will vary with the facility size and equivalent free-stream ambient conditions desired. Consequently, no clear-cut general conclusion regarding the use of simulation is possible, although the advantages of simulation increase as free-stream velocity or density (or both) increase.

Langley Research Center,
National Aeronautics and Space Administration,
Langley Station, Hampton, Va., January 21, 1966.

REFERENCES

1. Trimpi, Robert L.: A Preliminary Theoretical Study of the Expansion Tube, A New Device for Producing High-Enthalpy Short-Duration Hypersonic Gas Flows. NASA TR R-133, 1962.

2. Hertzberg, A.; Smith, W. E.; Glick, H. S.; and Squire, W.: Modifications of the Shock Tube for the Generation of Hypersonic Flow. AEDC-TN-55-15 (AD-789-A-2), Arnold Eng. Dev. Center, Mar. 1955.

3. Trimpi, Robert L.; and Callis, Linwood B.: A Perfect-Gas Analysis of the Expansion Tunnel, a Modification to the Expansion Tube. NASA TR R-223, 1965.

4. Norfleet, Glenn D.; and Loper, F. C.: A Theoretical Real Gas Analysis of the Expansion Tunnel. AEDC-TR 66-71, U.S. Air Force, June 1966.

5. Rose, P. H.; and Stark, W. I.: Stagnation Point Heat-Transfer Measurements in Dissociated Air. J. Aeron. Sci., vol. 25, no. 2, Feb. 1958, pp. 86-97.

6. Anon.: U.S. Standard Atmosphere, 1962. NASA, U.S. Air Force, and U.S. Weather Bur., Dec. 1962.

7. Little, Wanda J.: Mollier Diagram for Air. AEDC-TDR-63-190, U.S. Air Force, Sept. 1963.

8. Minzner, R. A.; Champion, K. S. W.; and Pond, H. L.: The ARDC Model Atmosphere, 1959. Air Force Surv. in Geophys. No. 115 (AFCRC-TR-59-267), Air Force Cambridge Res. Center, Aug. 1959.

9. Feldman, Saul: Hypersonic Gas Dynamic Charts for Equilibrium Air. Res. Rept. 40, Avco-Everett Res. Lab., Jan. 1957.

10. Moeckel, W. E.; and Weston, Kenneth C.: Composition and Thermodynamic Properties of Air in Chemical Equilibrium. NACA TN 4265, 1958.

11. Grose, William L.; and Trimpi, Robert L.: Charts for the Analysis of Isentropic One-Dimensional Unsteady Expansions in Equilibrium Real Air With Particular Reference to Shock-Initiated Flows. NASA TR R-167, 1963.

12. Wittliff, Charles E.; and Wilson, Merle R.: Shock Tube Driver Techniques and Attenuation Measurements. Rep. No. AD-1052-A-4 (Contract AF 18(603)-10), Cornell Aero. Lab., Inc., Aug. 1957.

13. Anon.: 24" Hypersonic Shock Tunnel. Cornell Aeron. Lab., Inc., Oct. 1959. (Rev. Jan. 1960.)

14. Sturgeon, R. B.; and Alford, D. E.: An Experimental Investigation of Internal Resistance Shock Tube Driver Gas Heating Systems. ER 7823 (Contract NAS 8-11,349), Lockheed-Georgia Co., Apr. 26, 1965.

15. Trimpi, Robert L.: A Preliminary Study of a New Device for Producing High-Enthalpy, Short-Duration Gas Flows. Advances in Hypervelocity Techniques, Arthur M. Krill, ed., Plenum Press, 1962, pp. 425-451.

16. Seiff, Alvin; and Sommer, Simon C.: An Investigation of Some Effects of Mach Number and Air Temperature on the Hypersonic Flow Over a Blunt Body. NASA MEMO 10-9-58A, 1959.

17. Seiff, Alvin; and Whiting, Ellis E.: A Correlation Study of the Bow-Wave Profiles of Blunt Bodies. NASA TN D-1148, 1962.

18. Callis, Linwood B.; and Kemper, Jane T.: A Program for Equilibrium Normal Shock and Stagnation Point Solutions for Arbitrary Gas Mixtures. NASA TN D-3215, 1966.

19. Inger, G. R.: Nonequilibrium Flow Behind Strong Shock Waves in a Dissociated Ambient Gas. Rept. SM-38936, Missile and Space Systems Eng., Douglas Aircraft Company, Inc., Jan. 2, 1962.

20. Camm, J. C.; Kivel, B.; Taylor, R. L; and Teare, J. D.: Absolute Intensity of Non-Equilibrium Radiation in Air and Stagnation Heating at High Altitudes. Res. Rept. 93 (AFBMD TR 60-184), Avco-Everett Res. Lab., Dec. 1959.

INDEX TO FIGURES

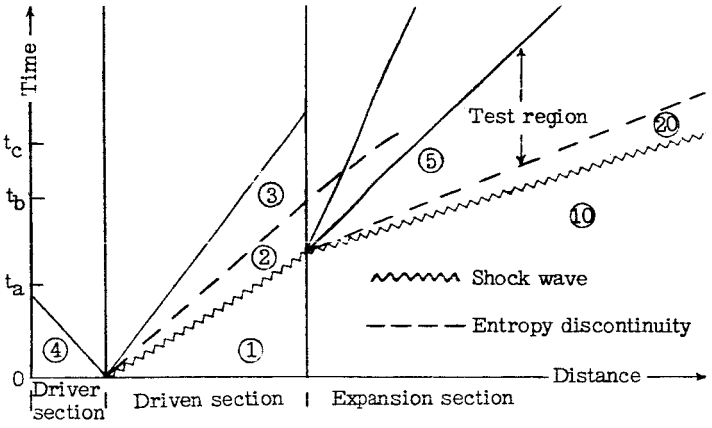

(a) Distance-time plot.

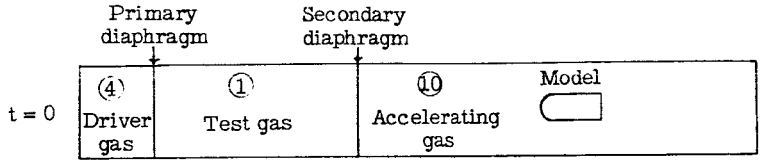

(b) Prior to run, $t = 0$.

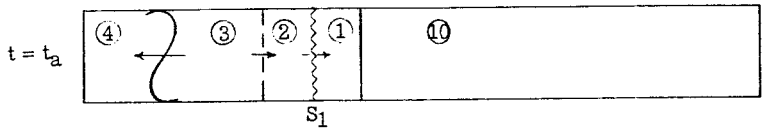

(c) After primary diaphragm burst, $t = t_a$.

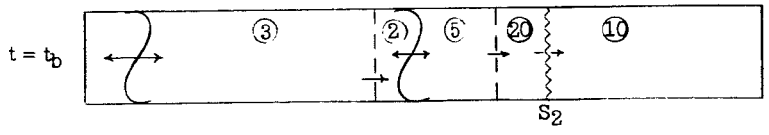

(d) After secondary diaphragm burst, $t = t_b$.

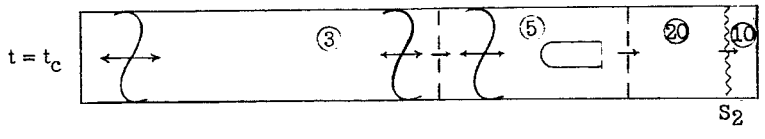

(e) During testing, $t = t_c$.

Figure 1.- Sketches illustrating expansion-tube cycle.

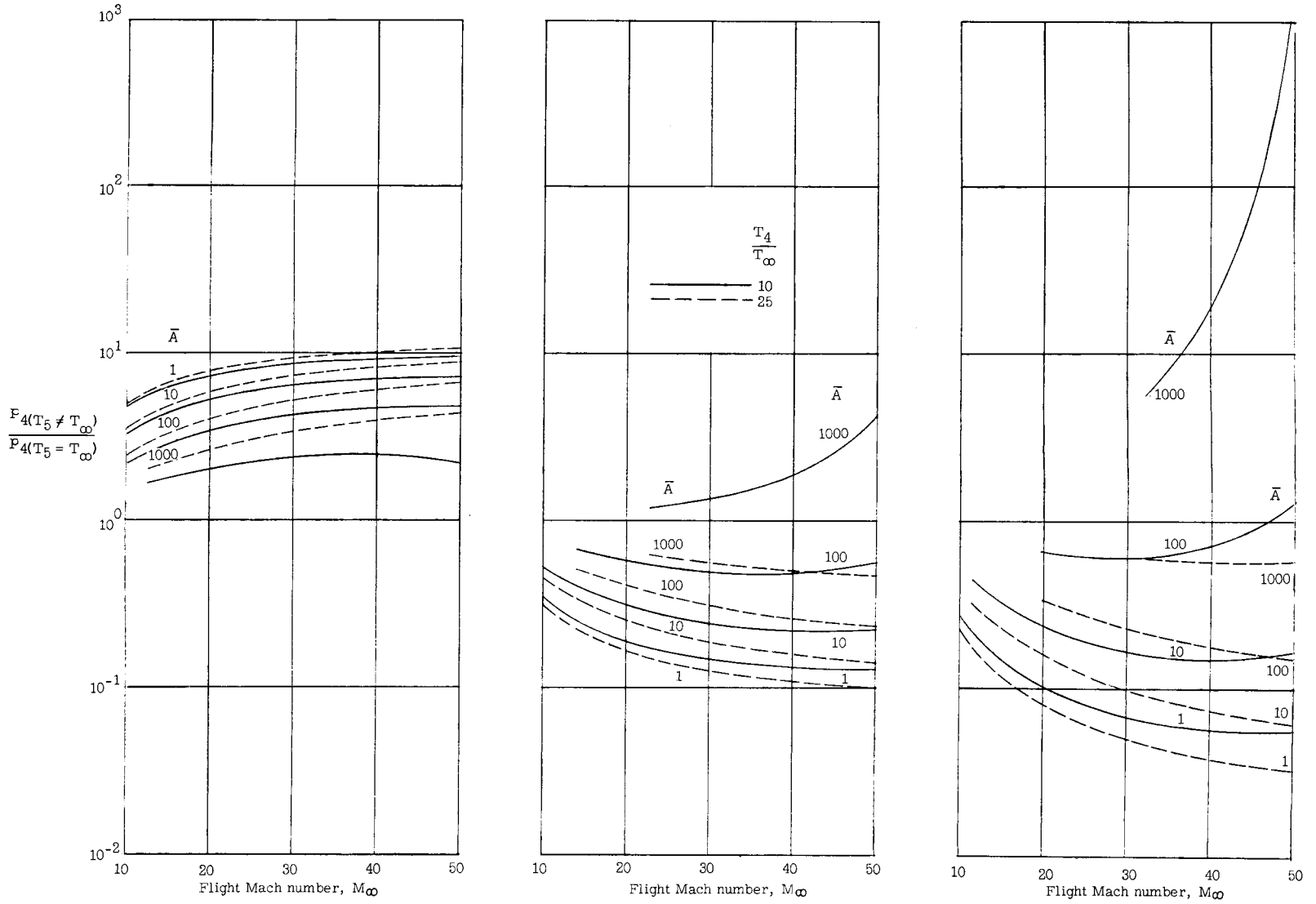

(a) $T_5/T_\infty = 1/3$.

(b) $T_5/T_\infty = 10/3$.

(c) $T_5/T_\infty = 20/3$.

Figure 2.- Variation in driver-pressure ratio for simulation with flight Mach number and area ratio. $\gamma_4 = 5/3$, $\gamma = 1.4$.

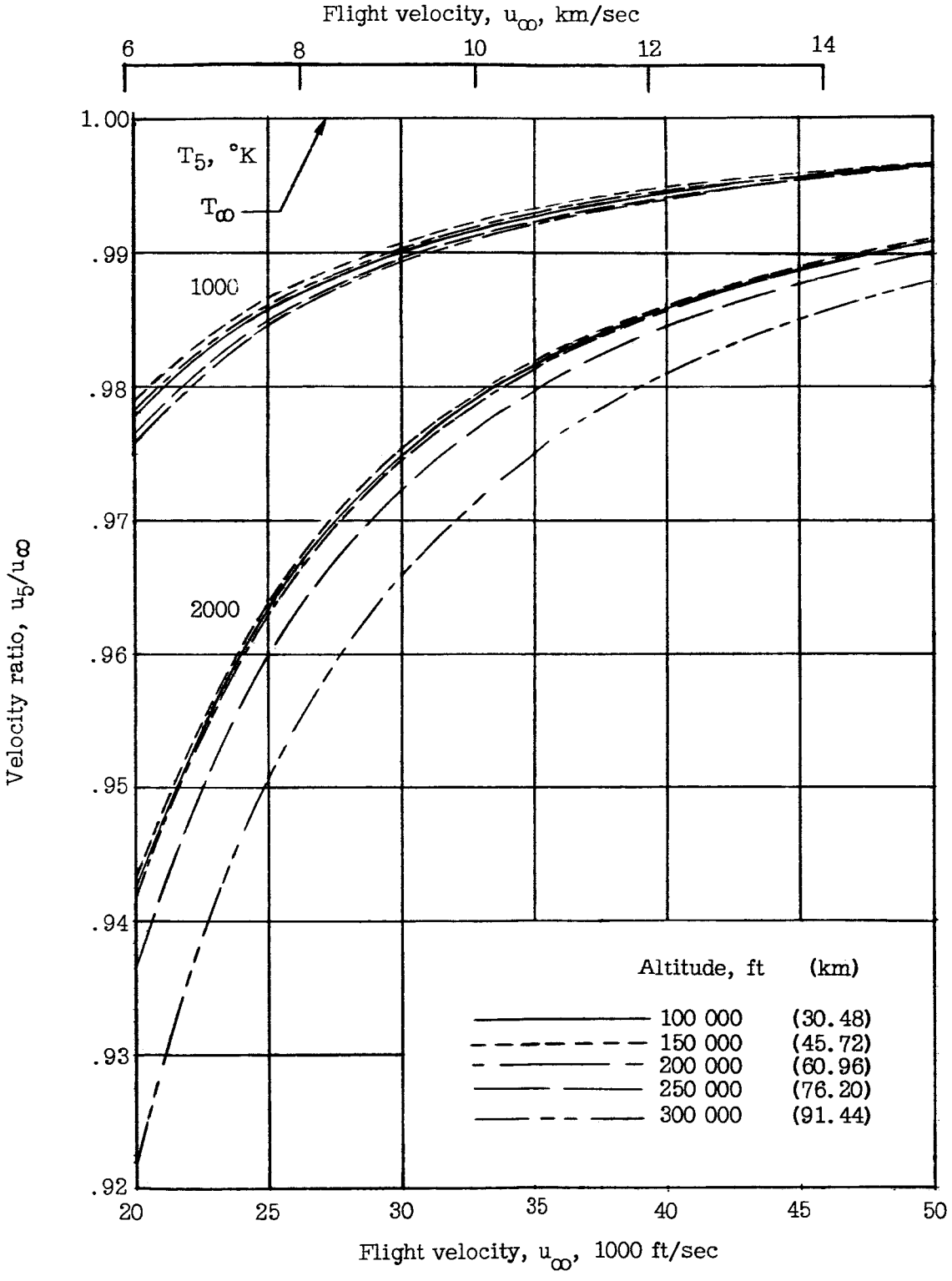

Figure 3.- Velocity ratio for simulation.

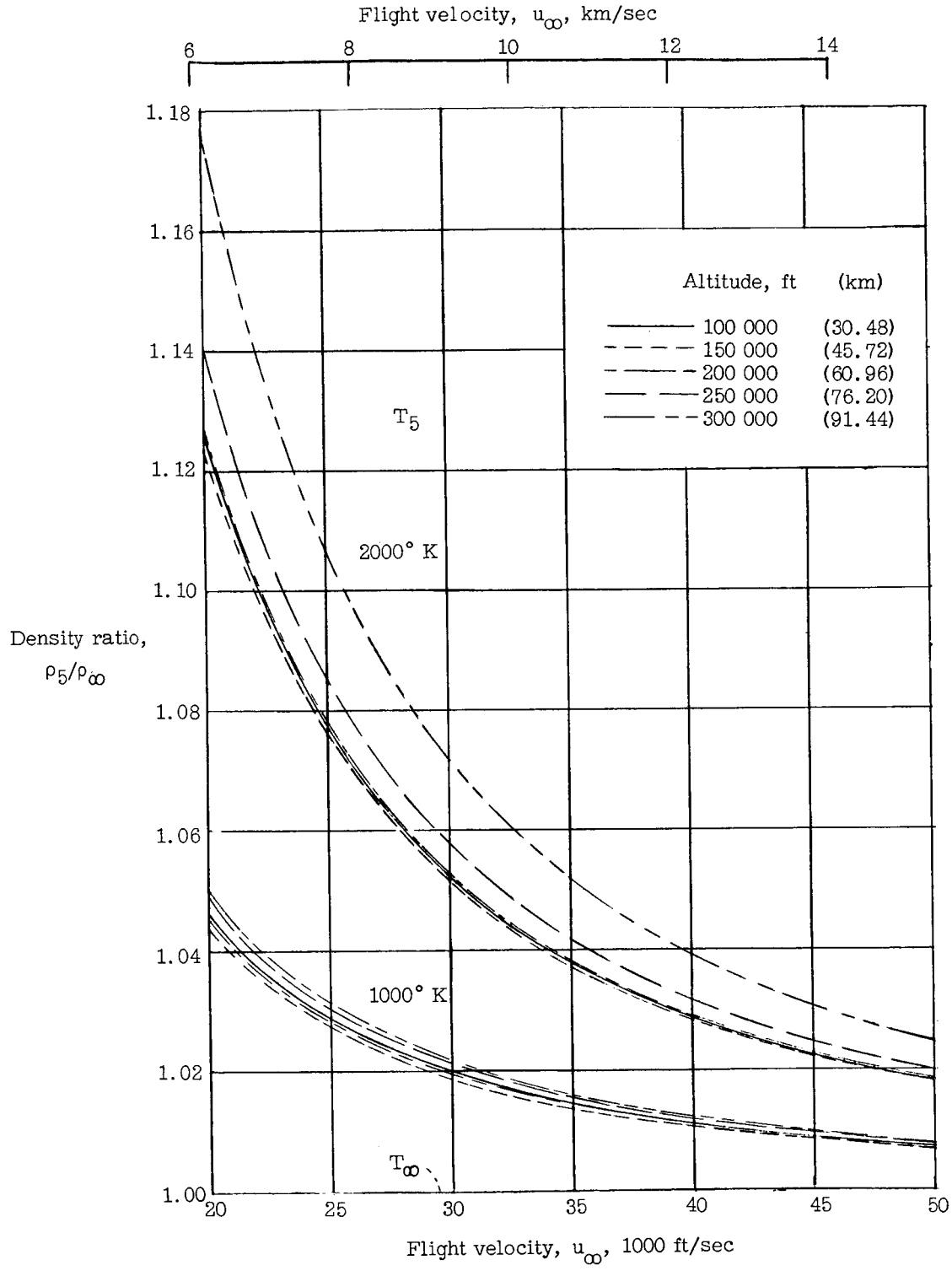

Figure 4.- Density ratio for simulation.

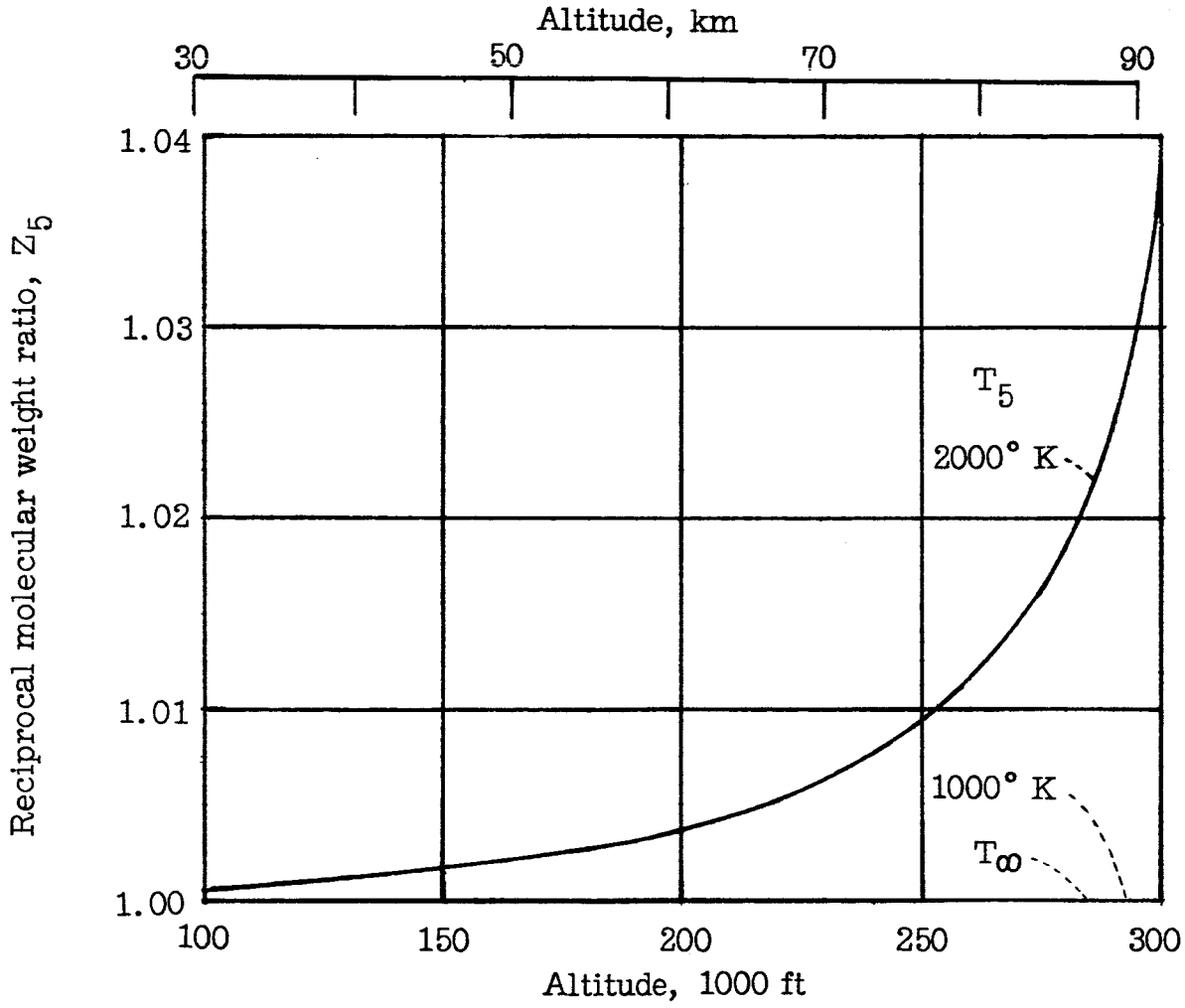

Figure 5.- Reciprocal molecular weight ratio Z_5 as a function of altitude.

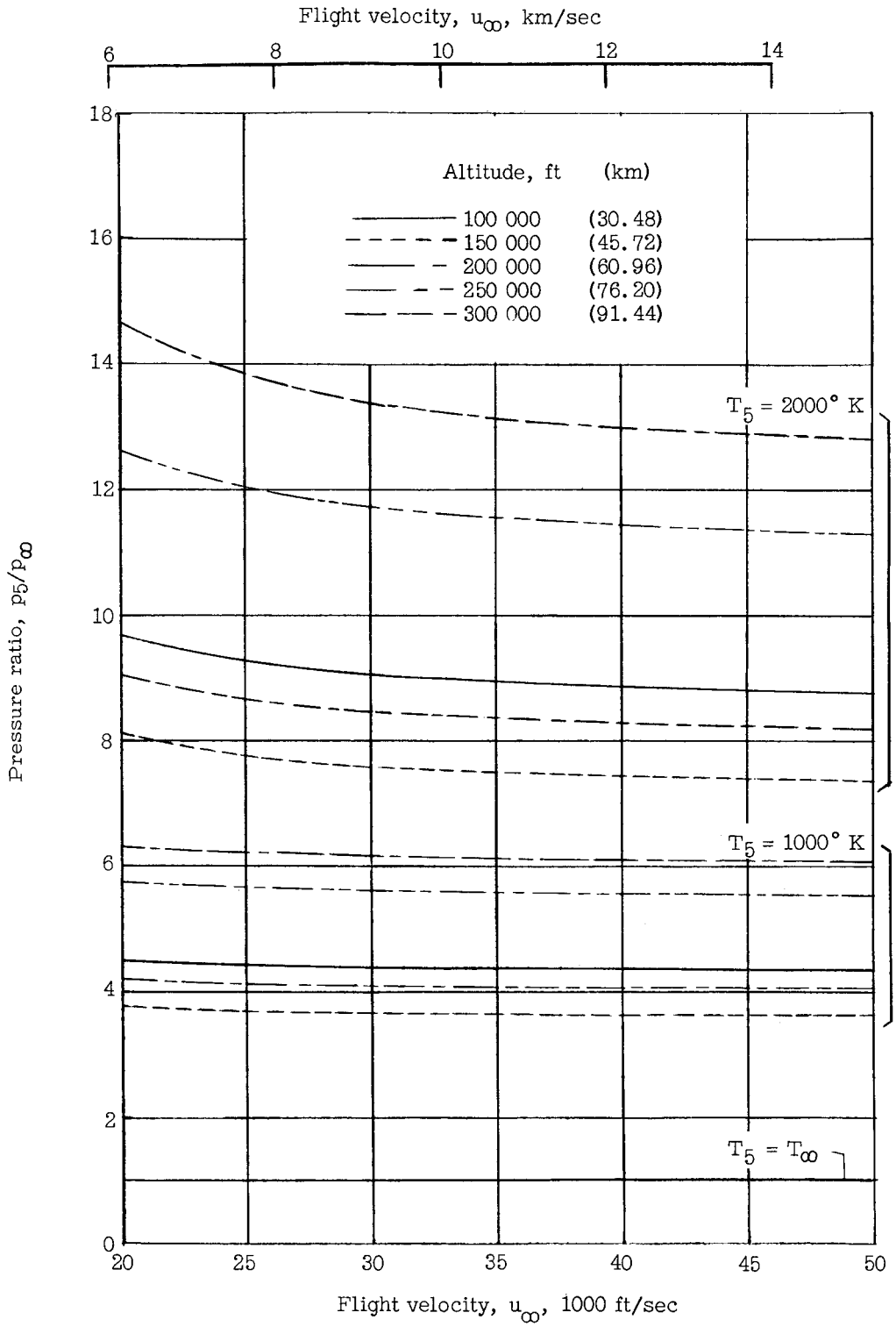

Figure 6.- Pressure ratio for simulation.

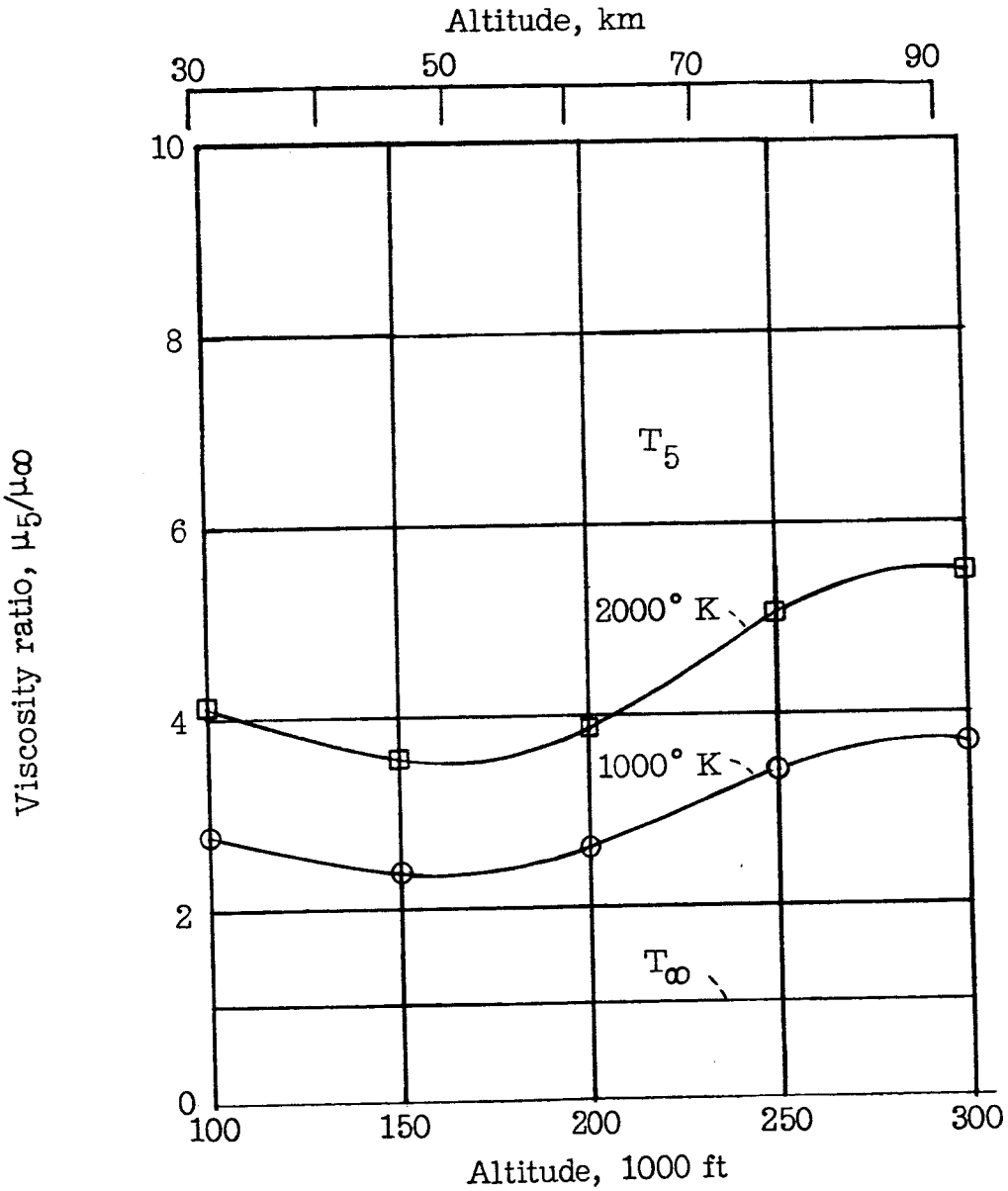

Figure 7.- Viscosity ratio for simulation.

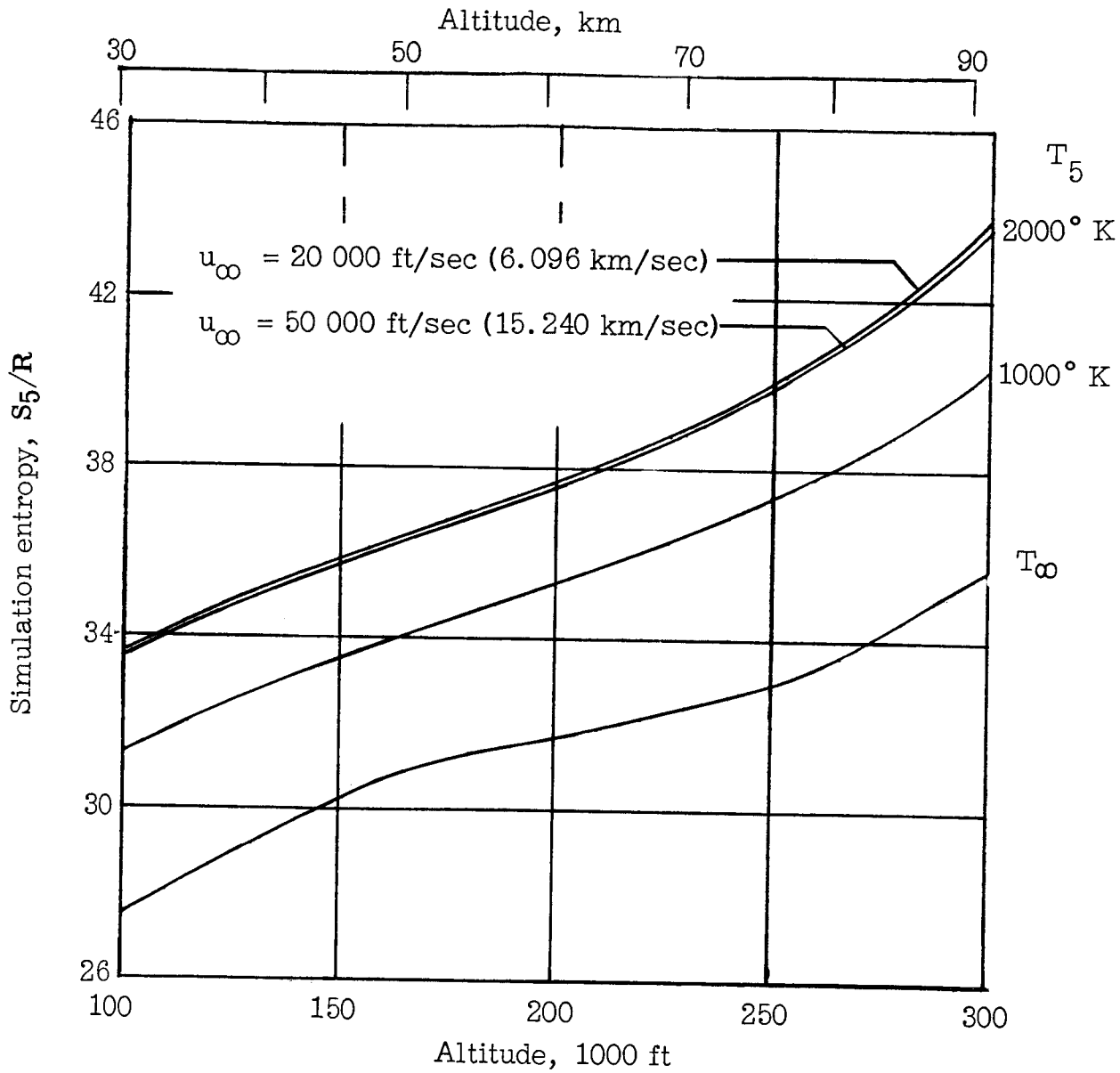

Figure 8.- Entropy variation with altitude for $T_5 = T_\infty$, 1000° K, and 2000° K.

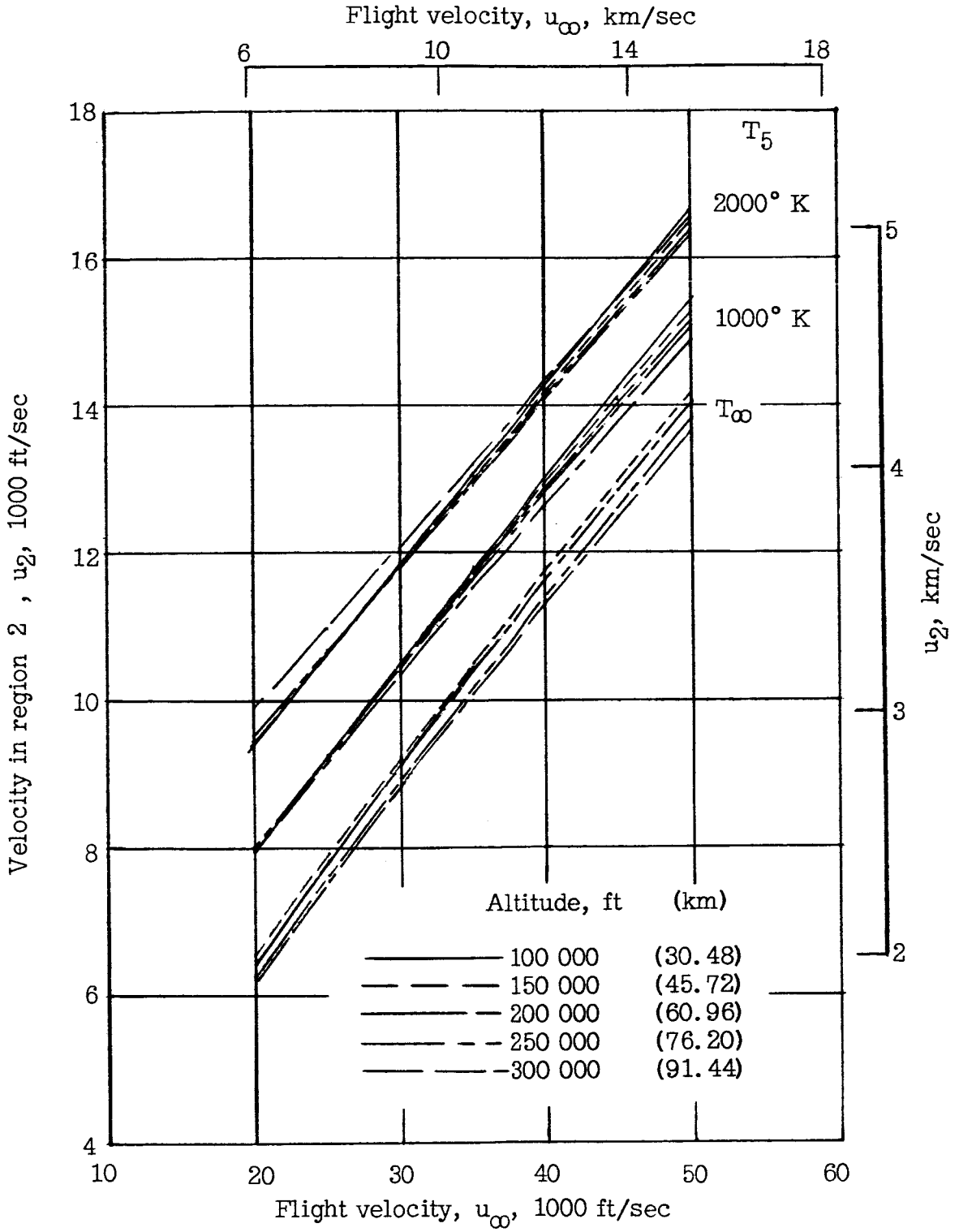

Figure 9.- Variation of u_2 with flight velocity.

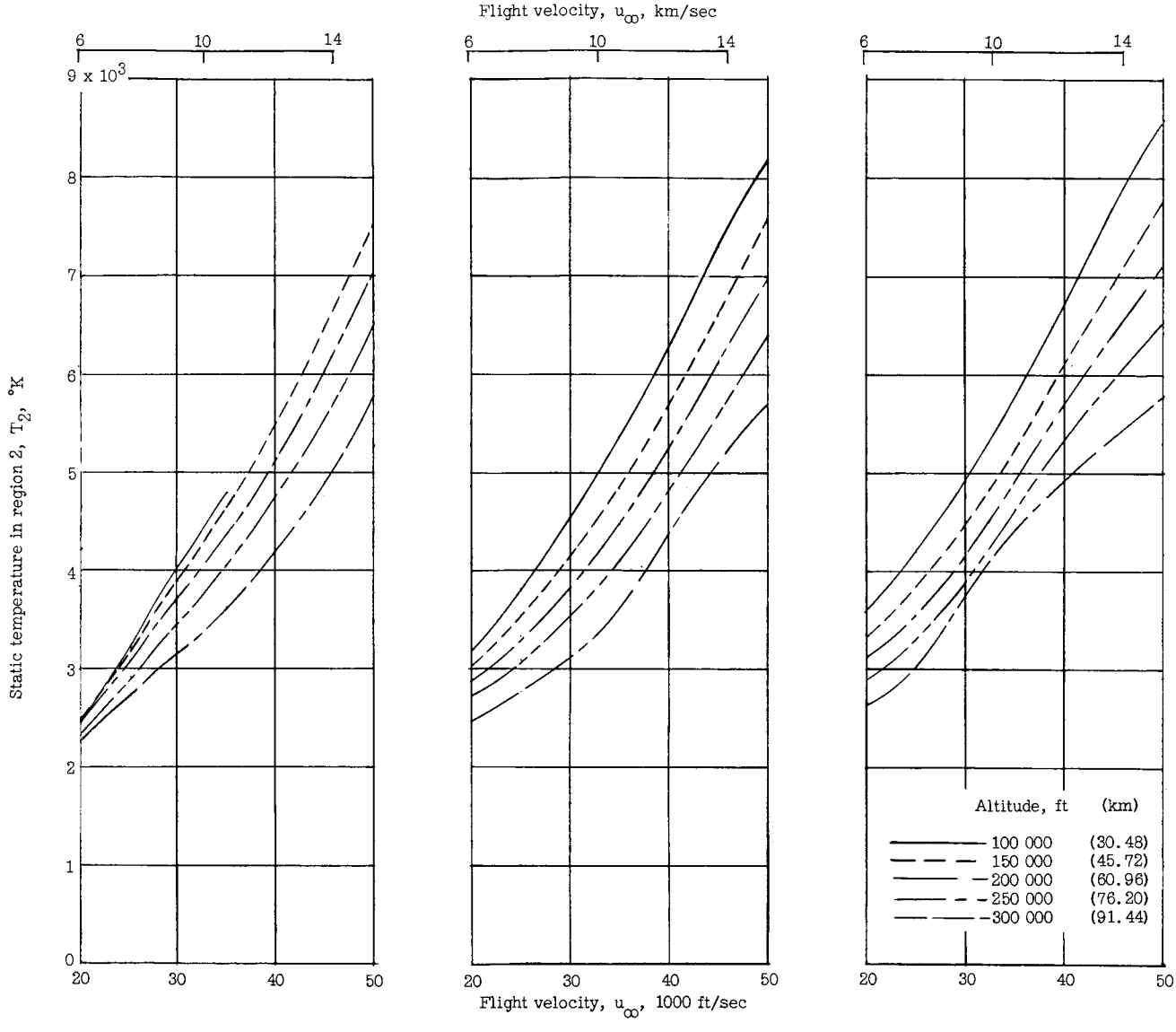

(a) $T_5 = T_\infty$.

(b) $T_5 = 1000^0$ K.

(c) $T_5 = 2000^0$ K.

Figure 10.- Variation of T_2 with flight velocity.

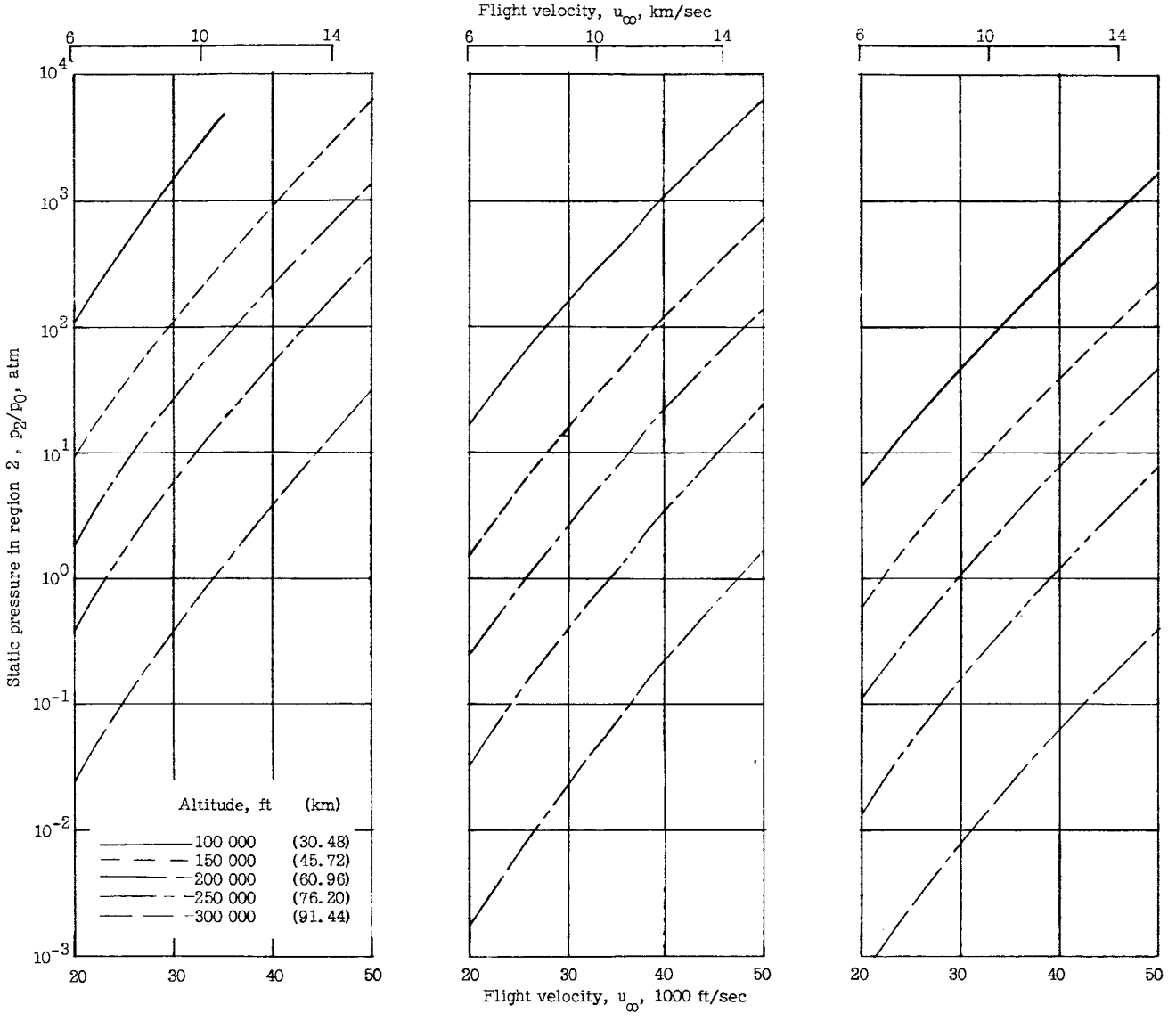

(a) $T_5 = T_\infty$.

(b) $T_5 = 1000^0$ K.

(c) $T_5 = 2000^0$ K.

Figure 11.- Variation of p_2 with flight velocity.

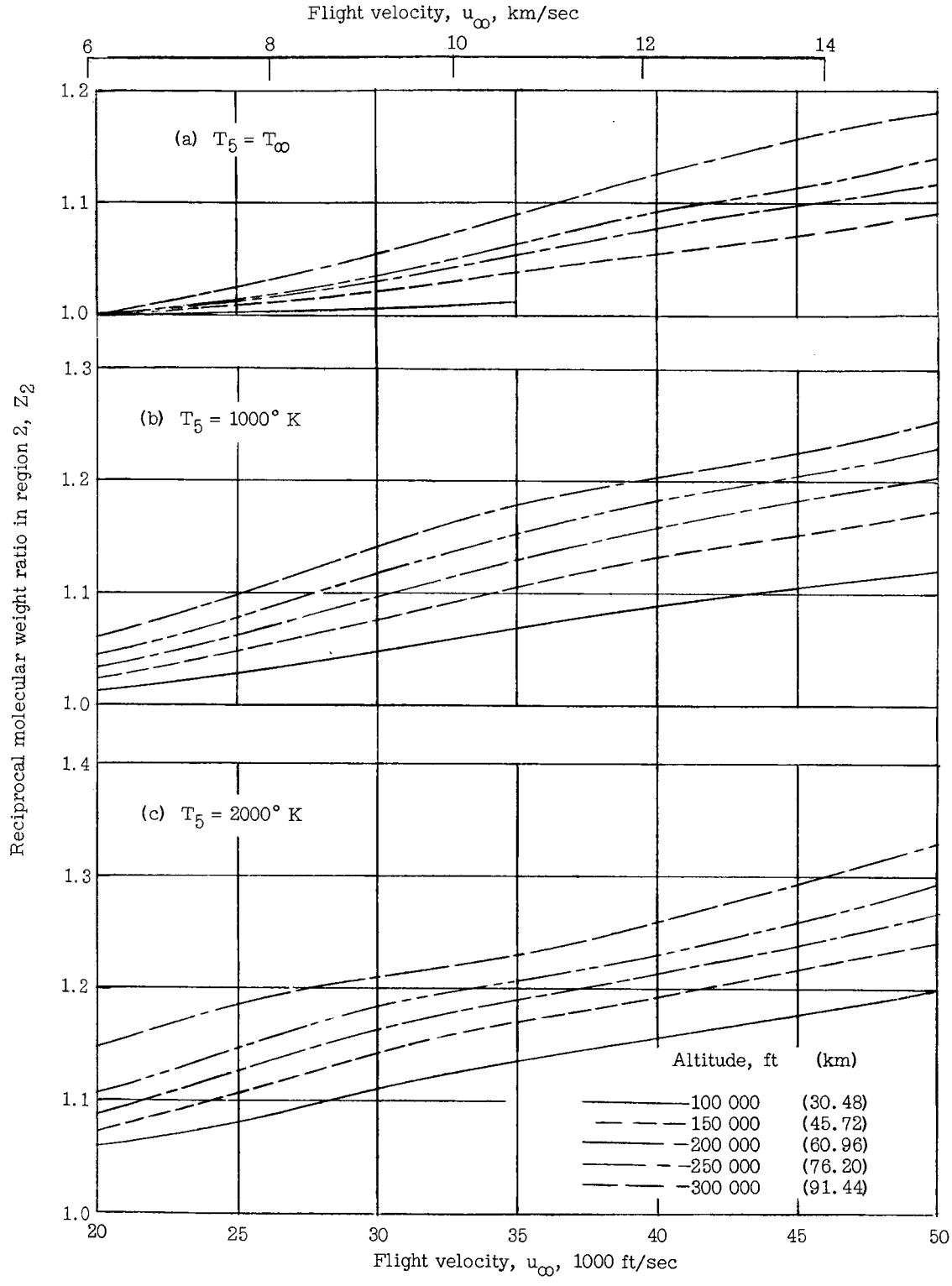

Figure 12.- Variation of reciprocal molecular weight ratio in region 2 with flight velocity.

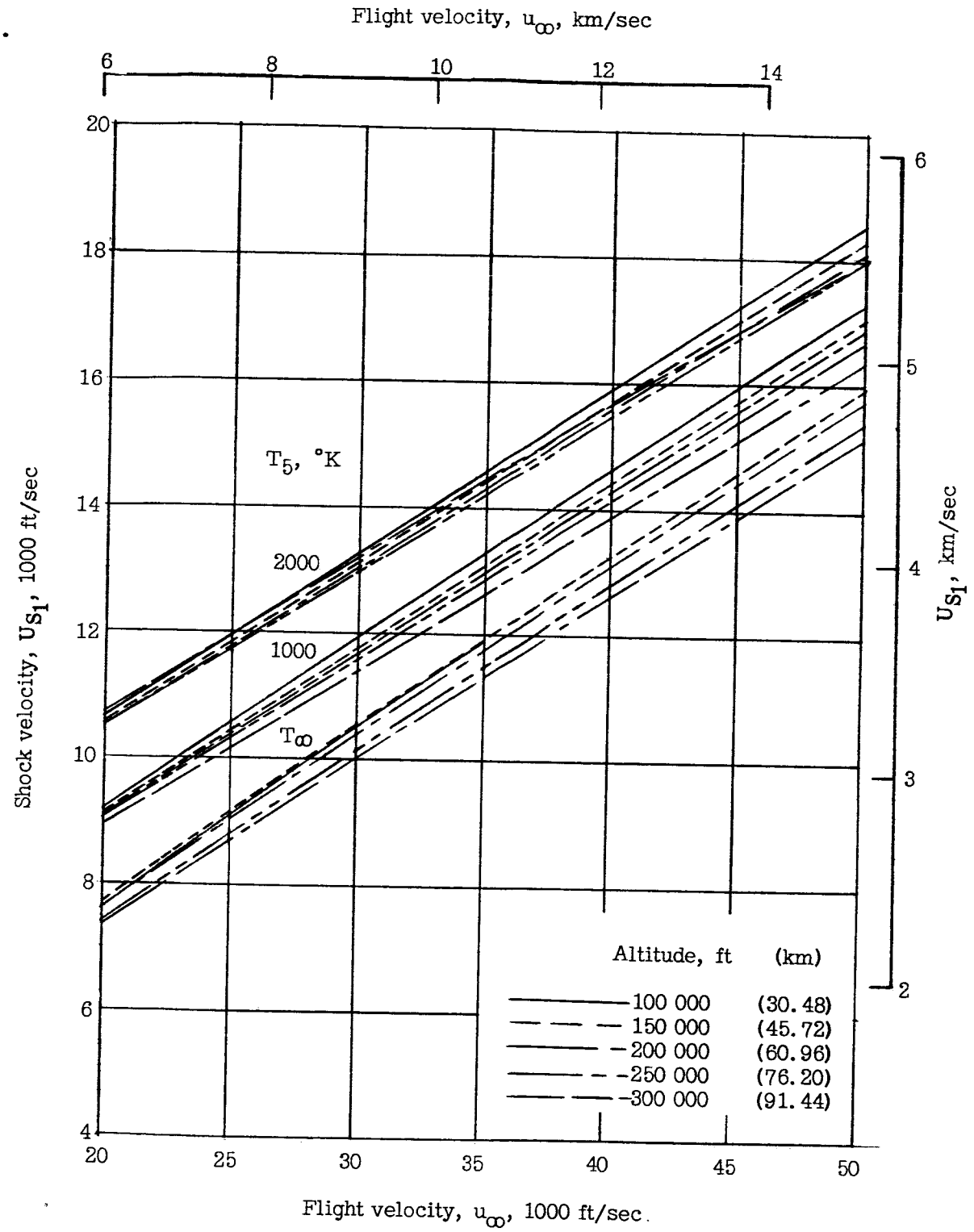

Figure 13.- Variation of shock velocity with flight velocity.

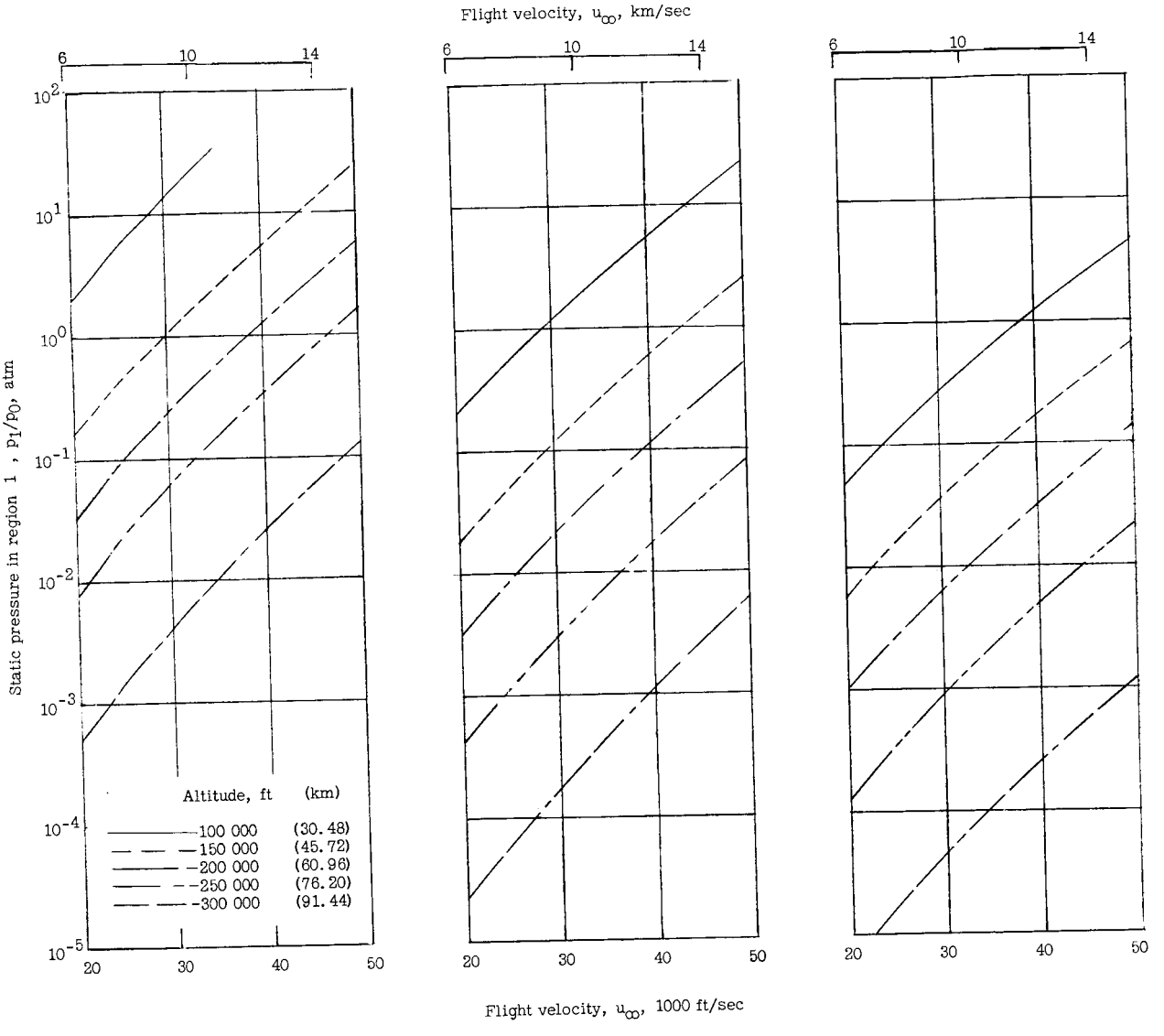

(a) $T_5 = T_\infty$.

(b) $T_5 = 1000^0$ K.

(c) $T_5 = 2000^0$ K.

Figure 14.- Variation of pressure in region 1 with flight velocity.

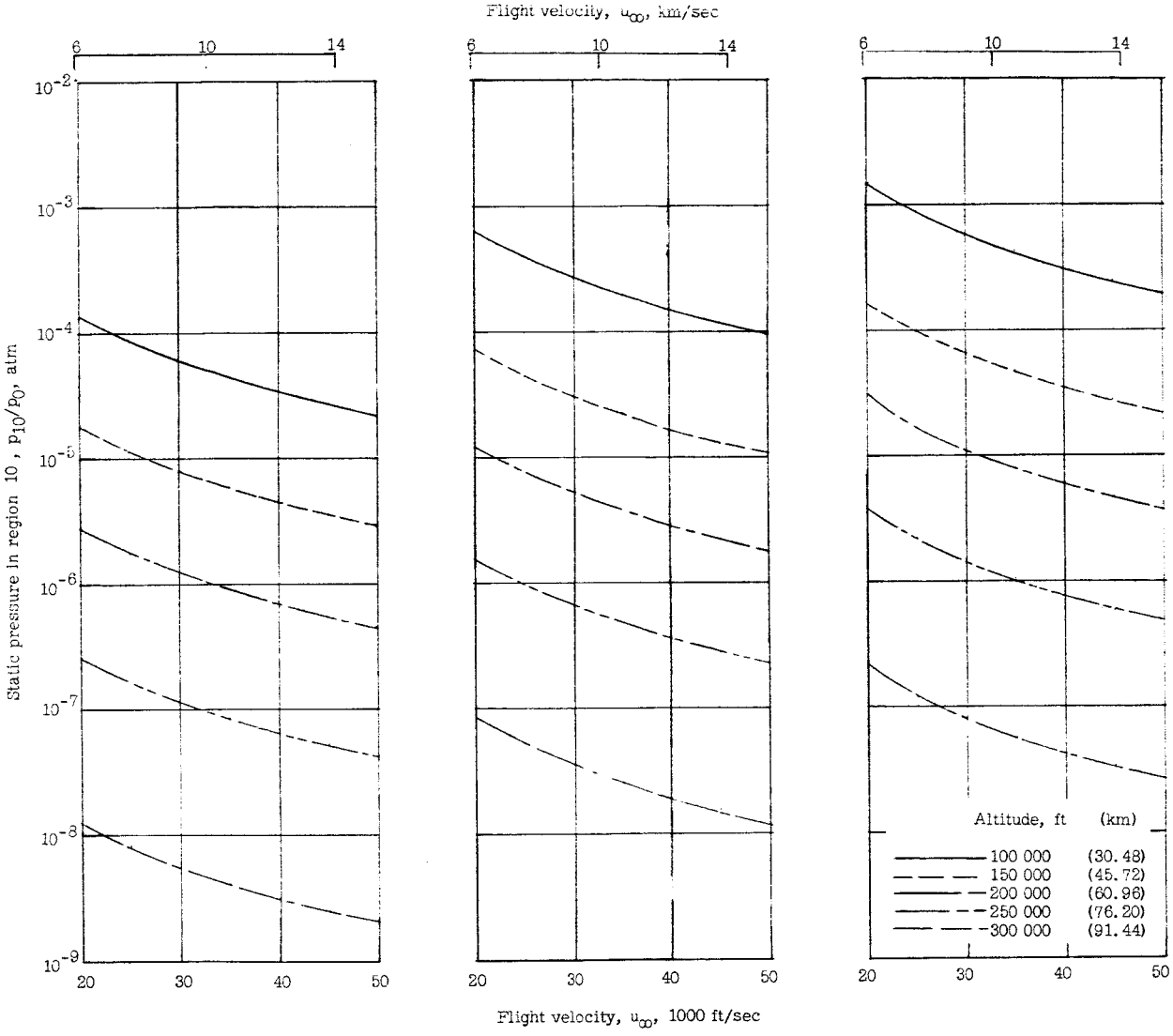

(a) $T_5 = T_\infty$.

(b) $T_5 = 1000^0$ K.

(c) $T_5 = 2000^0$ K.

Figure 15.- Variation of pressure in region 10 with flight velocity.

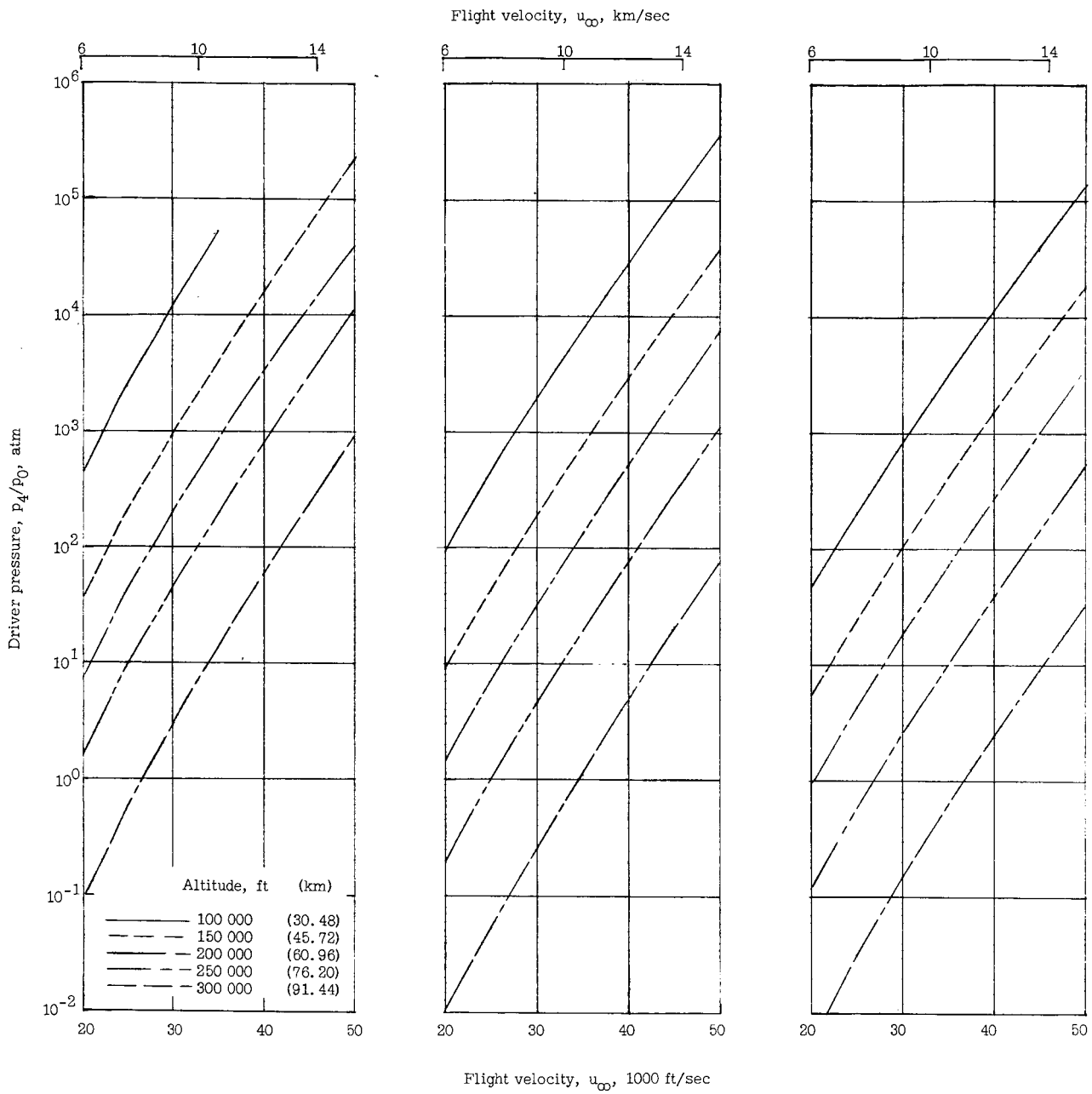

(a) $T_5 = T_\infty$.

(b) $T_5 = 1000^0$ K.

(c) $T_5 = 2000^0$ K.

Figure 16.- Variation of pressure in region 4 with flight velocity for combustion driver with 75 percent helium.

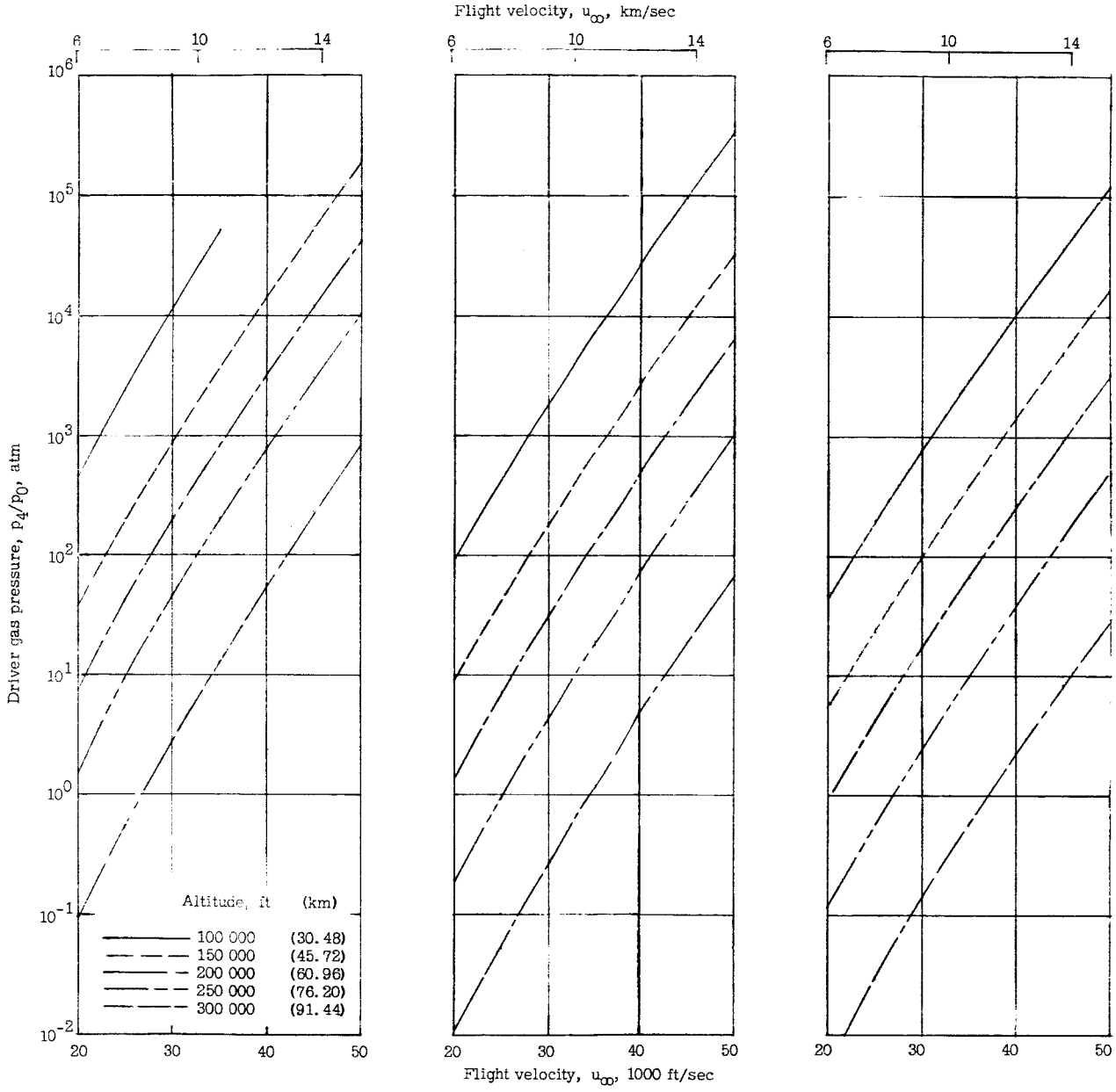

(a) $T_5 = T_\infty$.

(b) $T_5 = 1000^0$ K.

(c) $T_5 = 2000^0$ K.

Figure 17.- Variation of pressure in region 4 with flight velocity for hydrogen driver with $T_4 = 833^0$ K.

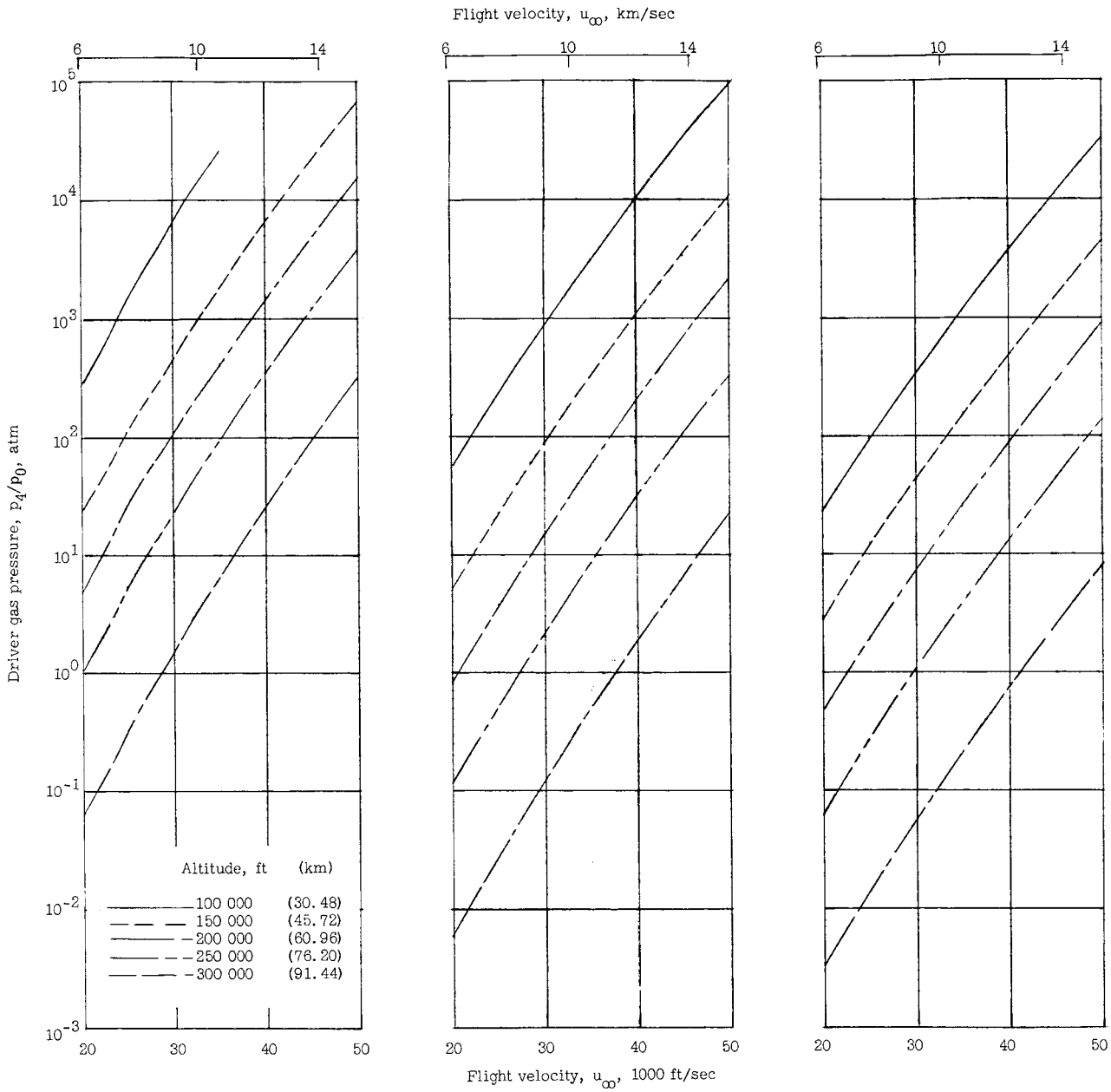

(a) $T_5 = T_\infty$.

(b) $T_5 = 1000^0$ K.

(c) $T_5 = 2000^0$ K.

Figure 18.- Variation of pressure in region 4 with flight velocity for helium driver with $T_4 = 4000^0$ K.

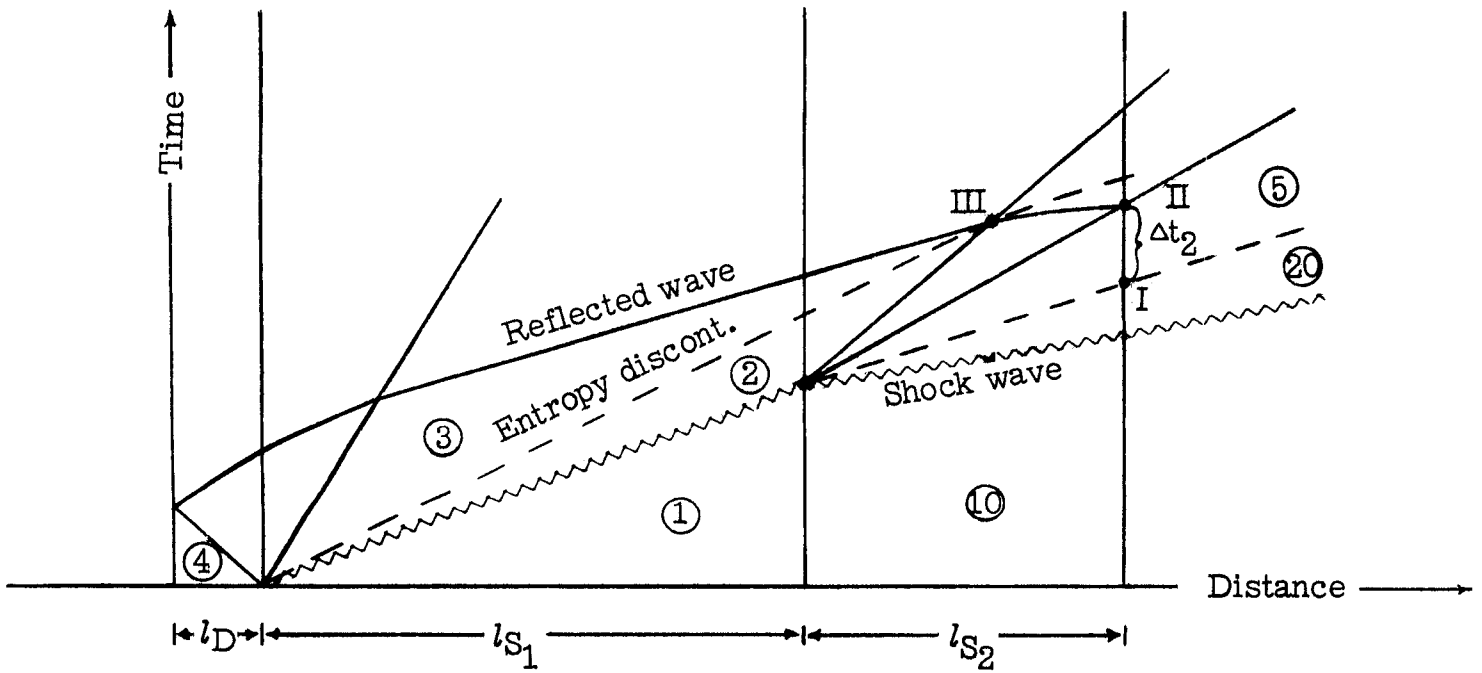

Figure 19.- Wave diagram of expansion tube illustrating determination of various section lengths.

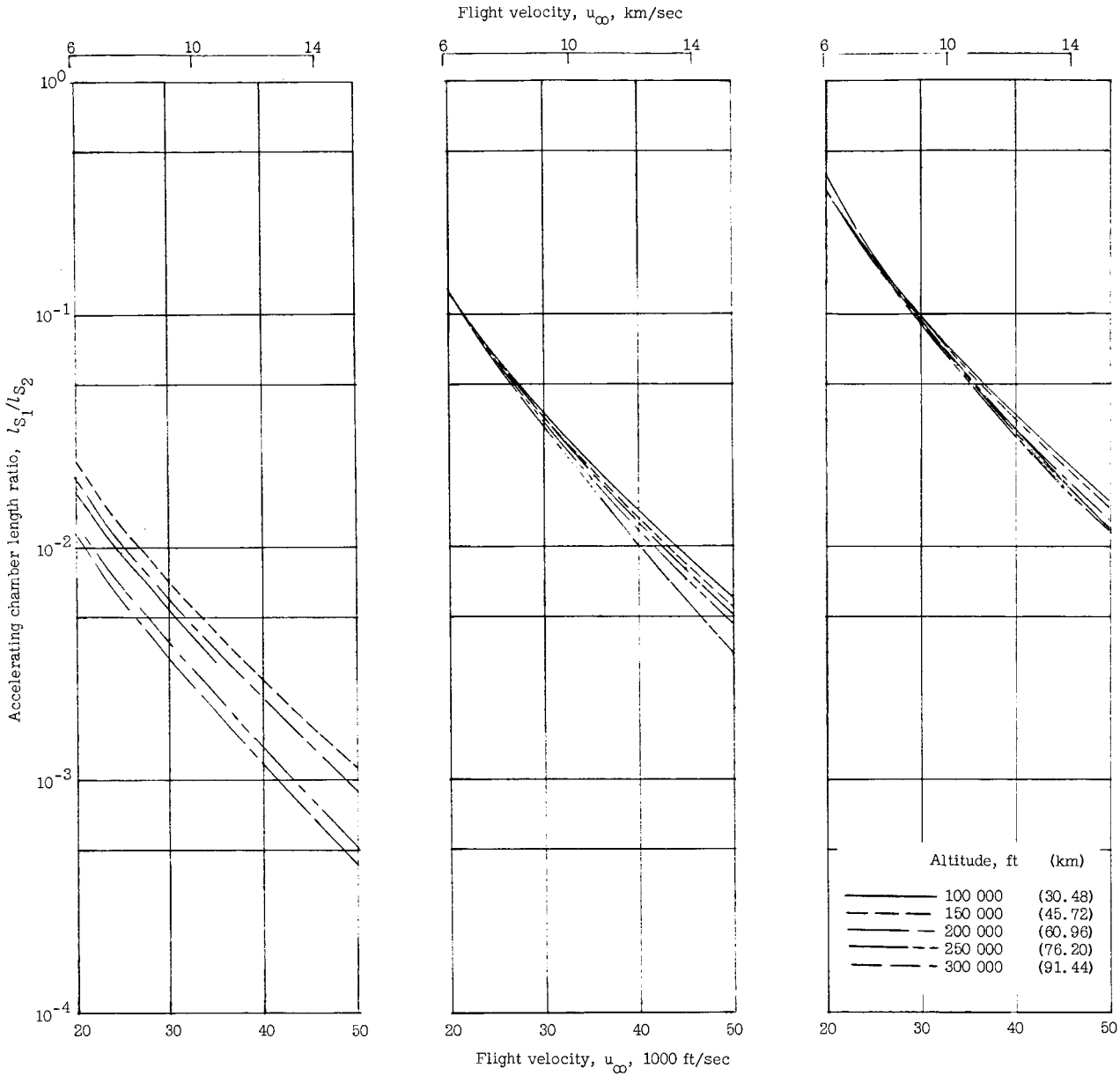

(a) $T_5 = T_\infty$.

(b) $T_5 = 1000^0$ K.

(c) $T_5 = 2000^0$ K.

Figure 20.- Variation of accelerating chamber length ratio with flight velocity.

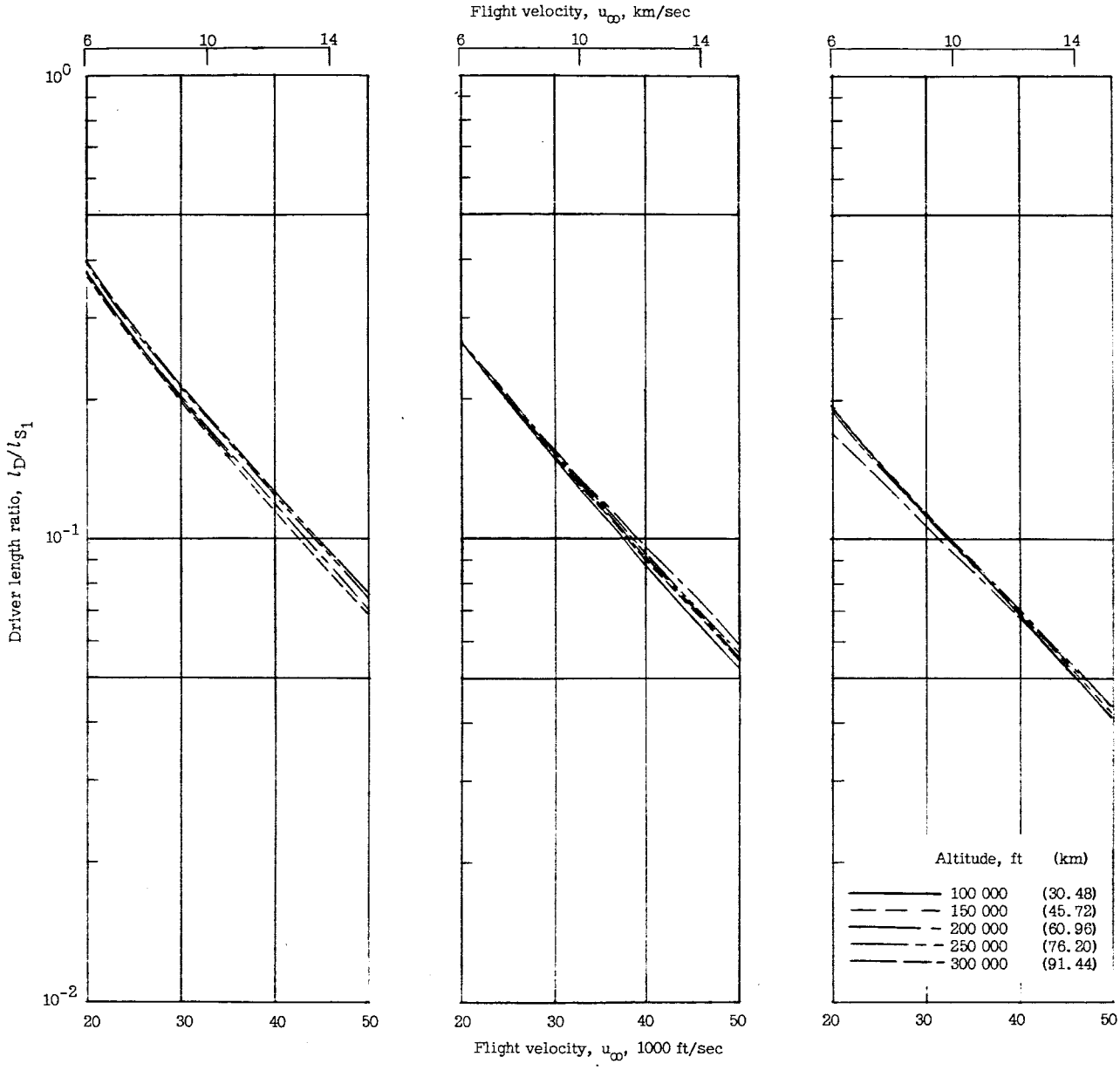

(a) $T_5 = T_\infty$.

(b) $T_5 = 1000^0$ K.

(c) $T_5 = 2000^0$ K.

Figure 21.- Driver length ratio variation with flight velocity for combustion driver with 75 percent helium.

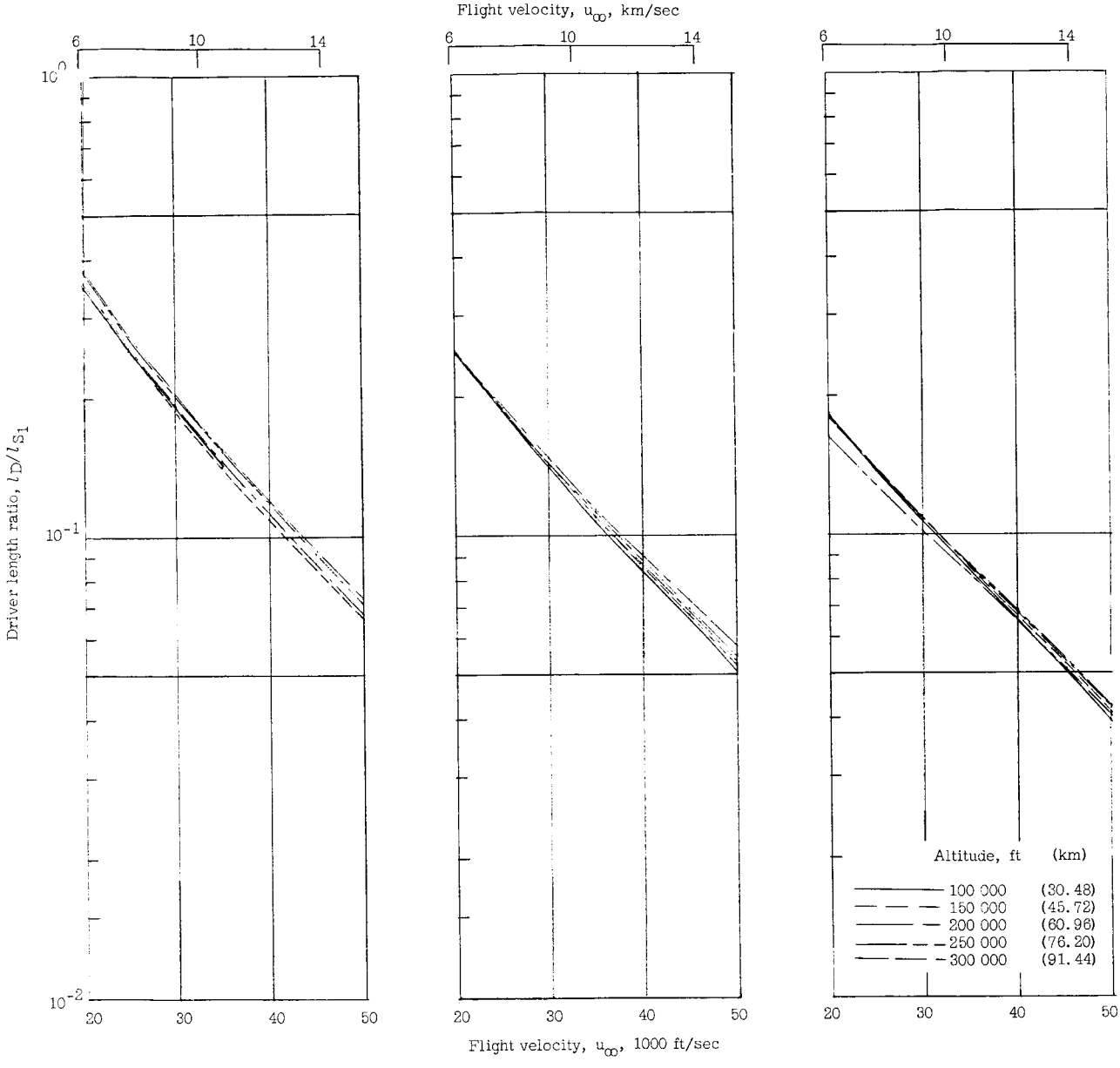

(a) $T_5 = T_\infty$.

(b) $T_5 = 1000^0$ K.

(c) $T_5 = 2000^0$ K.

Figure 22.- Driver length ratio variation with flight velocity for hydrogen driver with $T_4 = 833^0$ K.

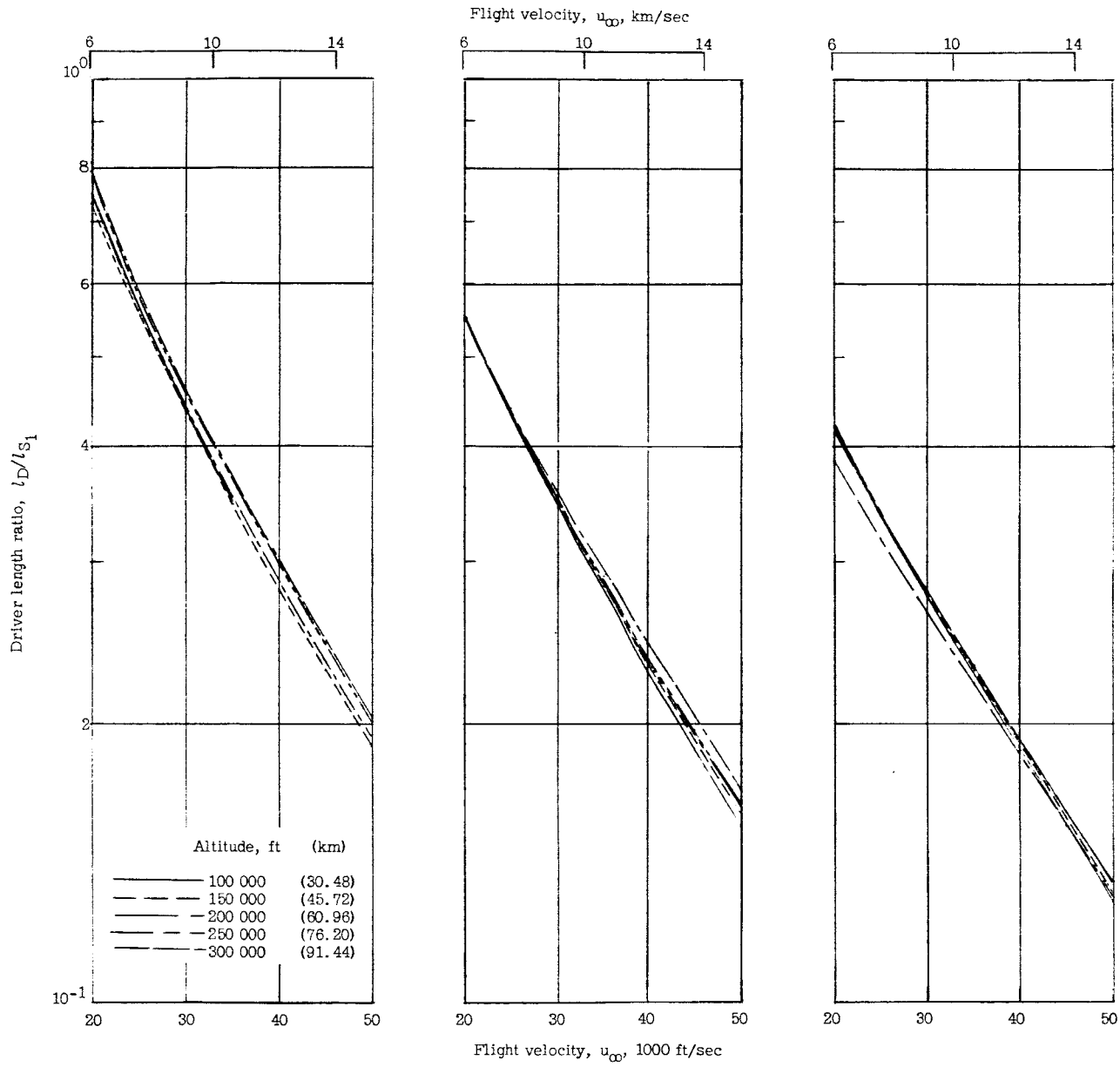

(a) $T_5 = T_\infty$.

(b) $T_5 = 1000^0$ K.

(c) $T_5 = 2000^0$ K.

Figure 23.- Driver length ratio variation with flight velocity for helium driver with $T_4 = 4000^0$ K.

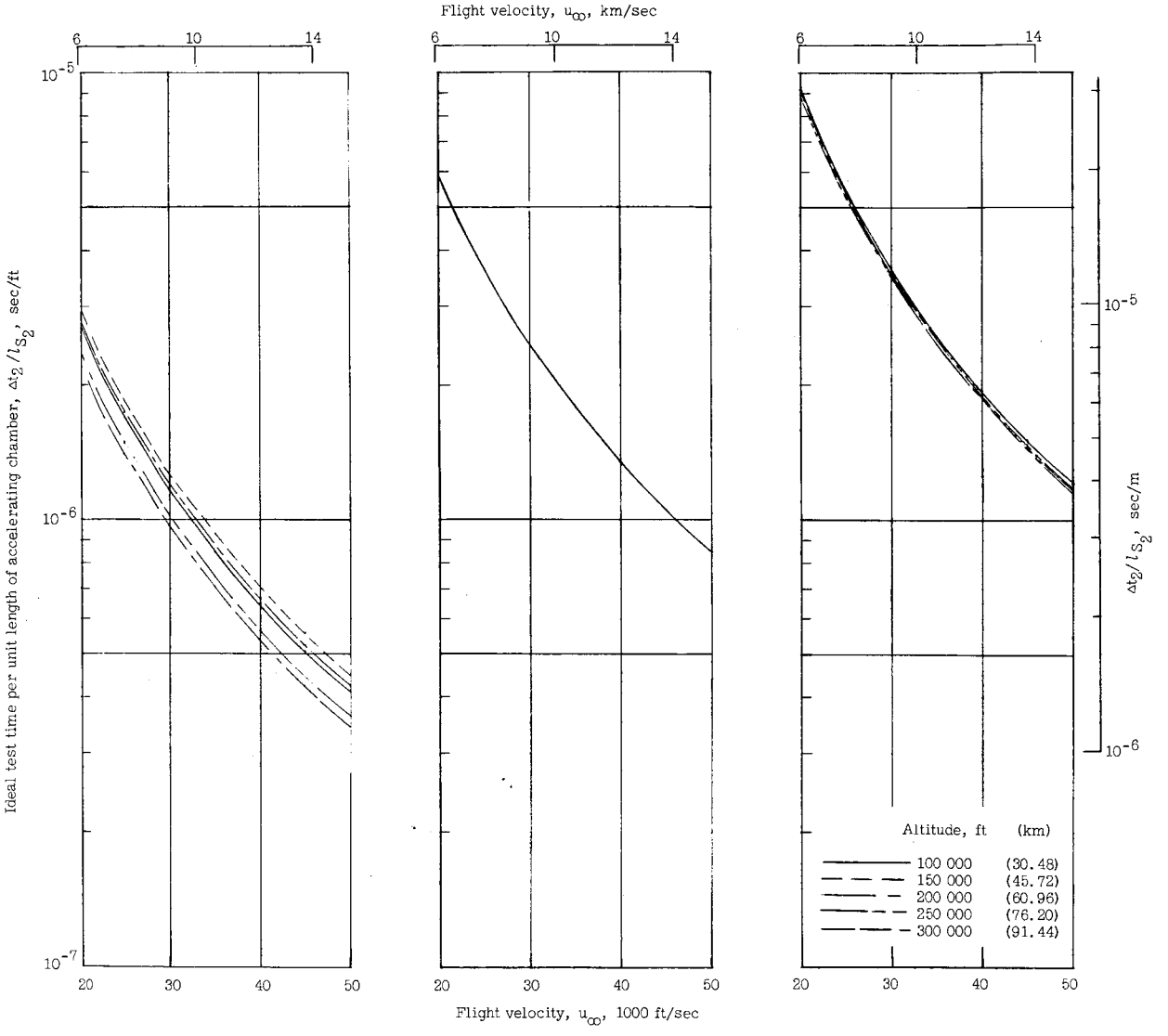

(a) $T_5 = T_\infty$.

(b) $T_5 = 1000^0$ K.

(c) $T_5 = 2000^0$ K.

Figure 24.- Variation of ideal test time per unit accelerating chamber length with flight velocity.

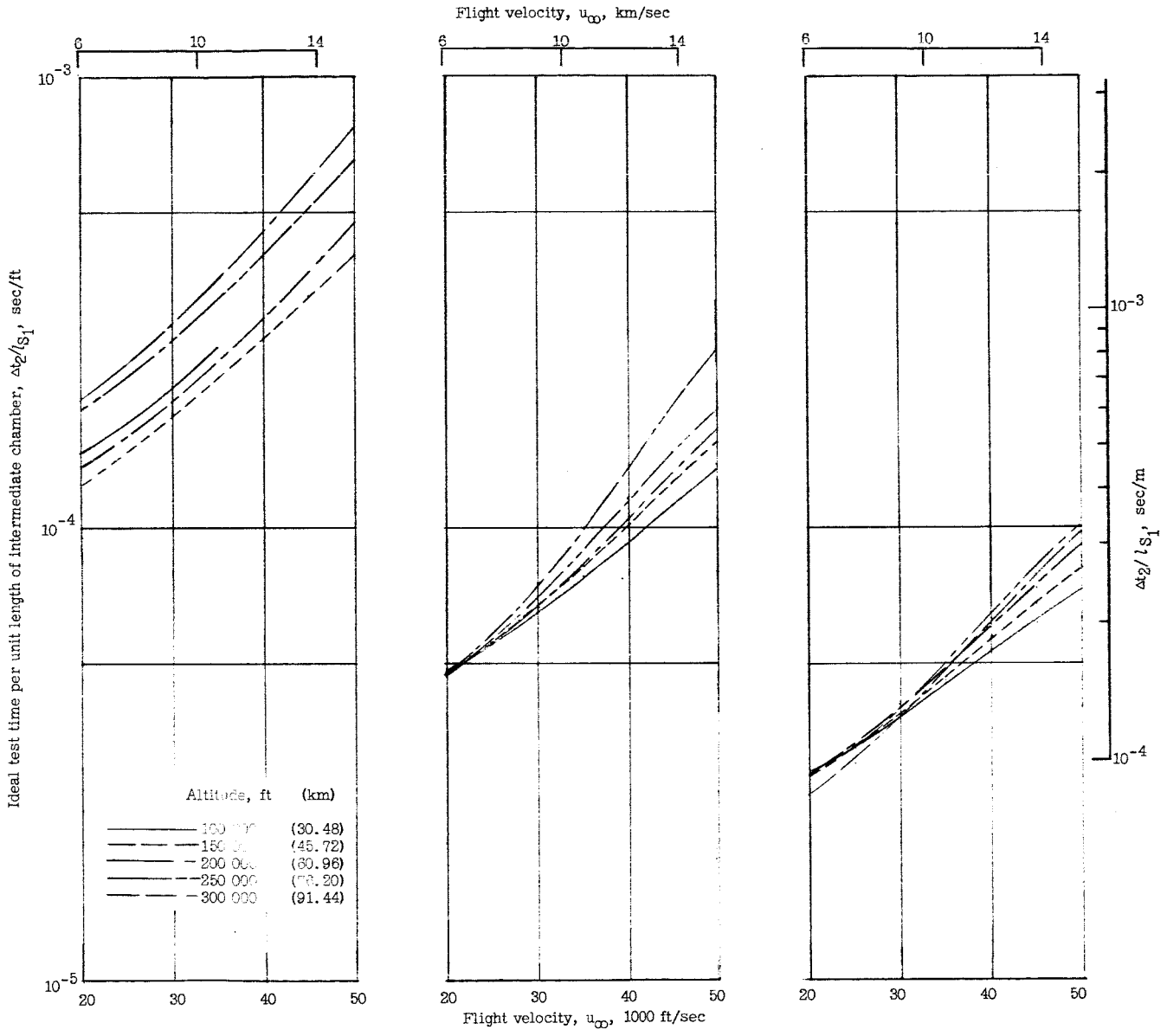

(a) $T_5 = T_\infty$.

(b) $T_5 = 1000^0$ K.

(c) $T_5 = 2000^0$ K.

Figure 25.- Variation of ideal test time per unit intermediate chamber length with flight velocity.

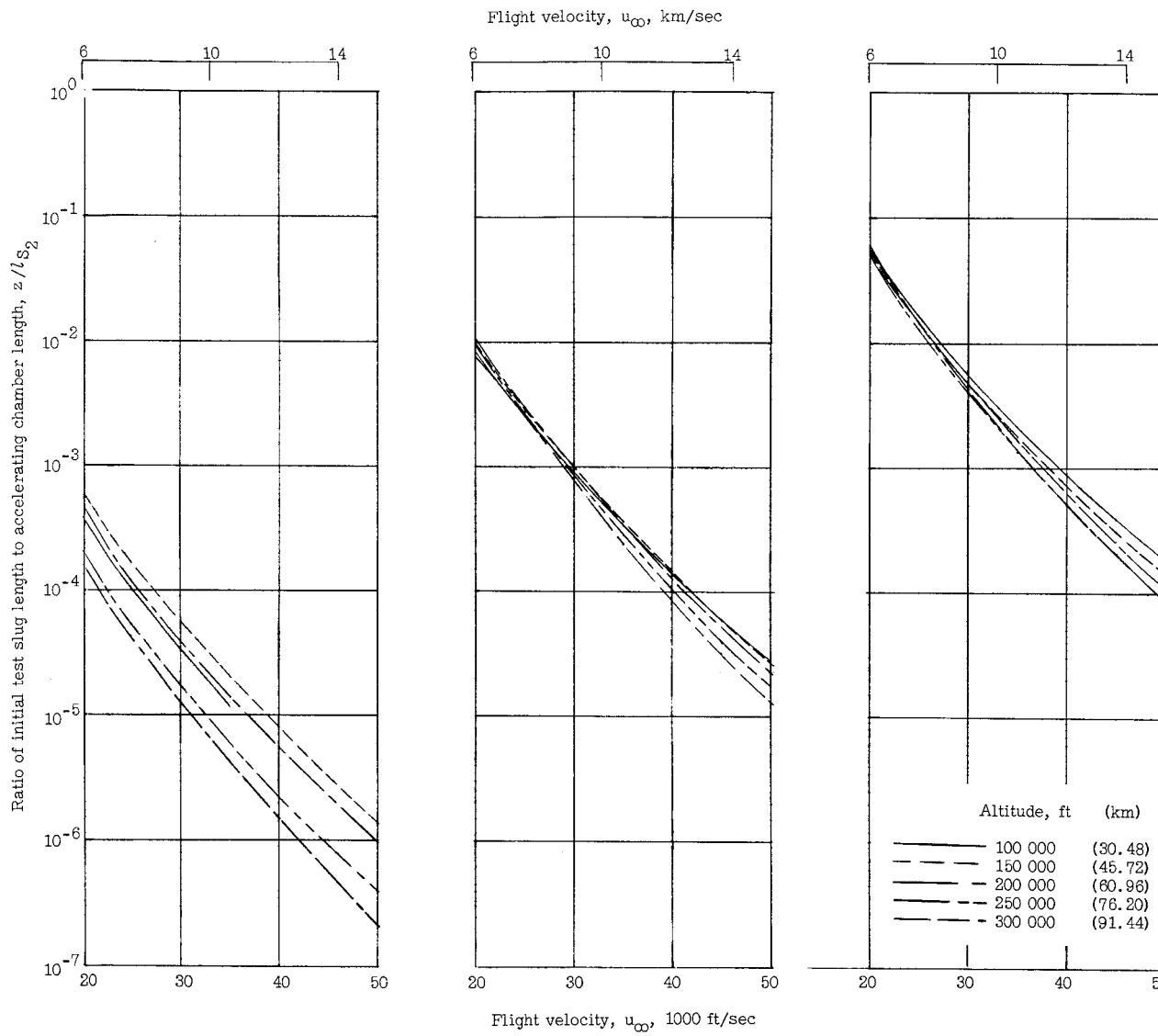

(a) $T_5 = T_\infty$.

(b) $T_5 = 1000^0$ K.

(c) $T_5 = 2000^0$ K.

Figure 26.- Variation of initial test slug length with flight velocity.

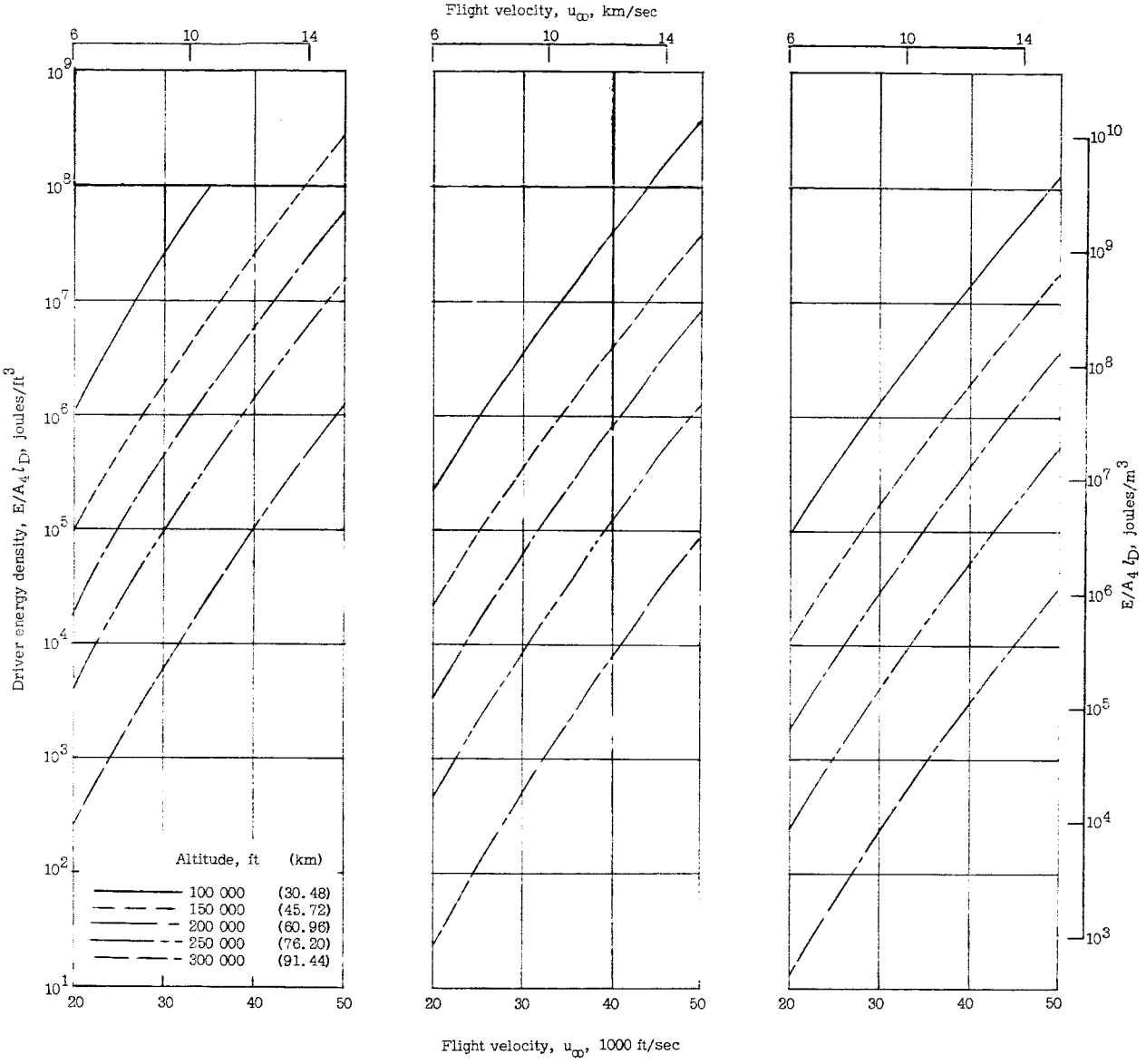

(a) $T_5 = T_\infty$.

(b) $T_5 = 1000^0$ K.

(c) $T_5 = 2000^0$ K.

Figure 27.- Variation of driver energy density with flight velocity for helium driver with $T_4 = 4000^0$ K.

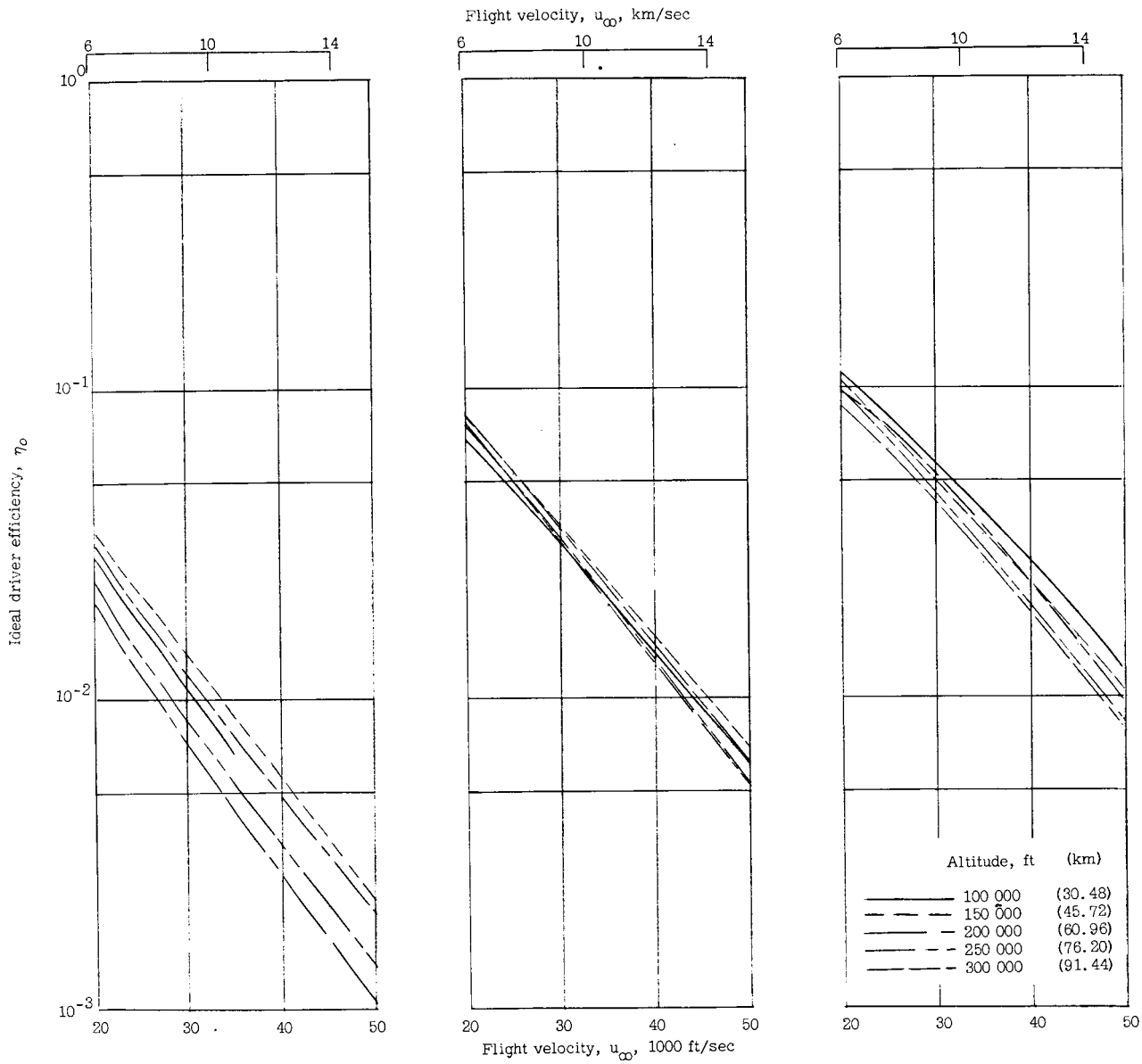

(a) $T_5 = T_\infty$.

(b) $T_5 = 1000^0$ K.

(c) $T_5 = 2000^0$ K.

Figure 28.- Variation of ideal driver efficiency with flight velocity for helium driver with $T_4 = 4000^0$ K.

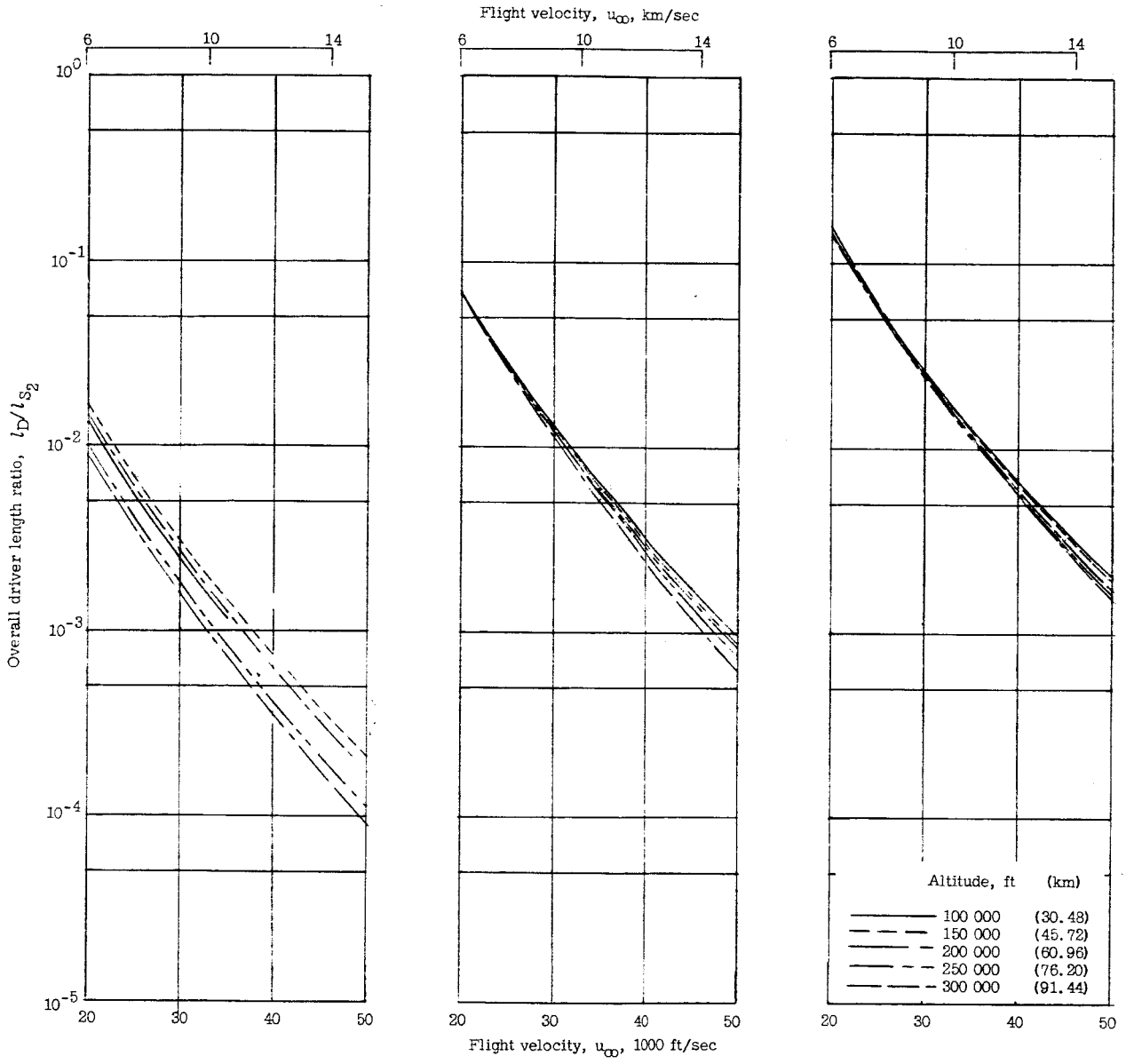

(a) $T_5 = T_\infty$ (b) $T_5 = 1000^0$ K. (c) $T_5 = 2000^0$ K.

Figure 29.- Variation of overall driver length ratio with flight velocity for helium driver with $T_4 = 4000^0$ K.

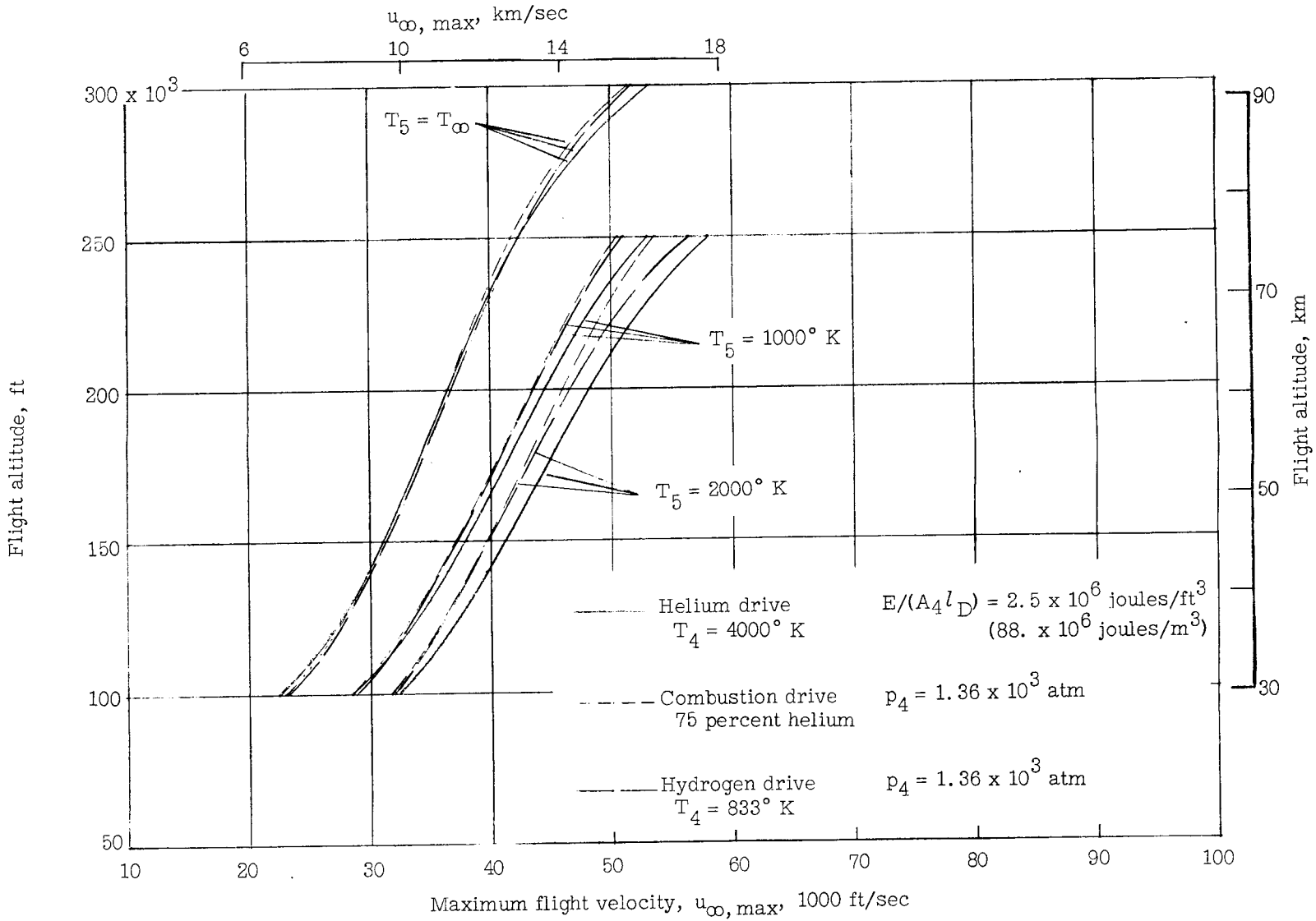

Figure 30.- Effect of simulation on maximum velocity capability of expansion tube using three typical driver modes.

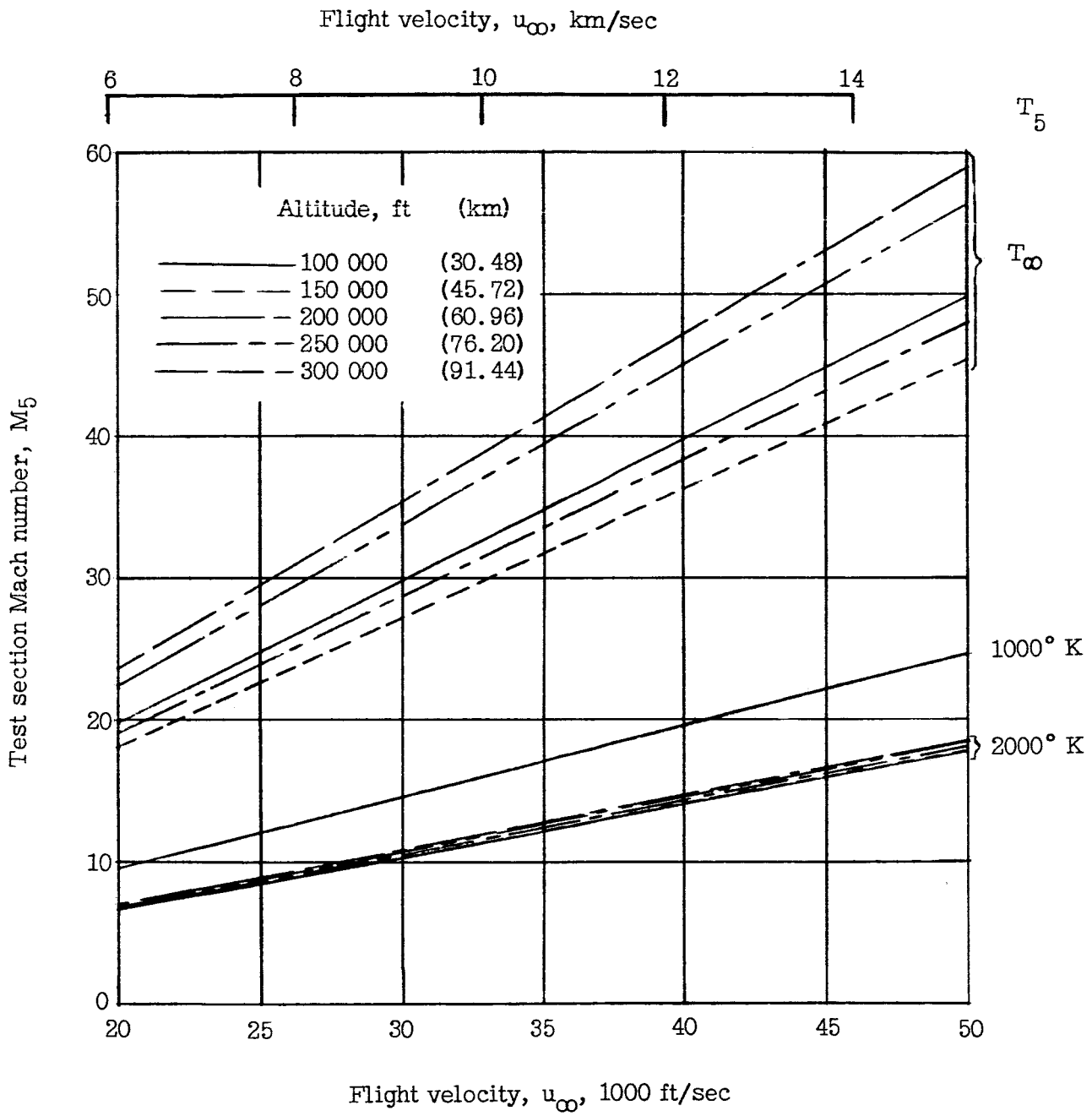

Figure 31.- Variation in test-section Mach number with flight velocity.

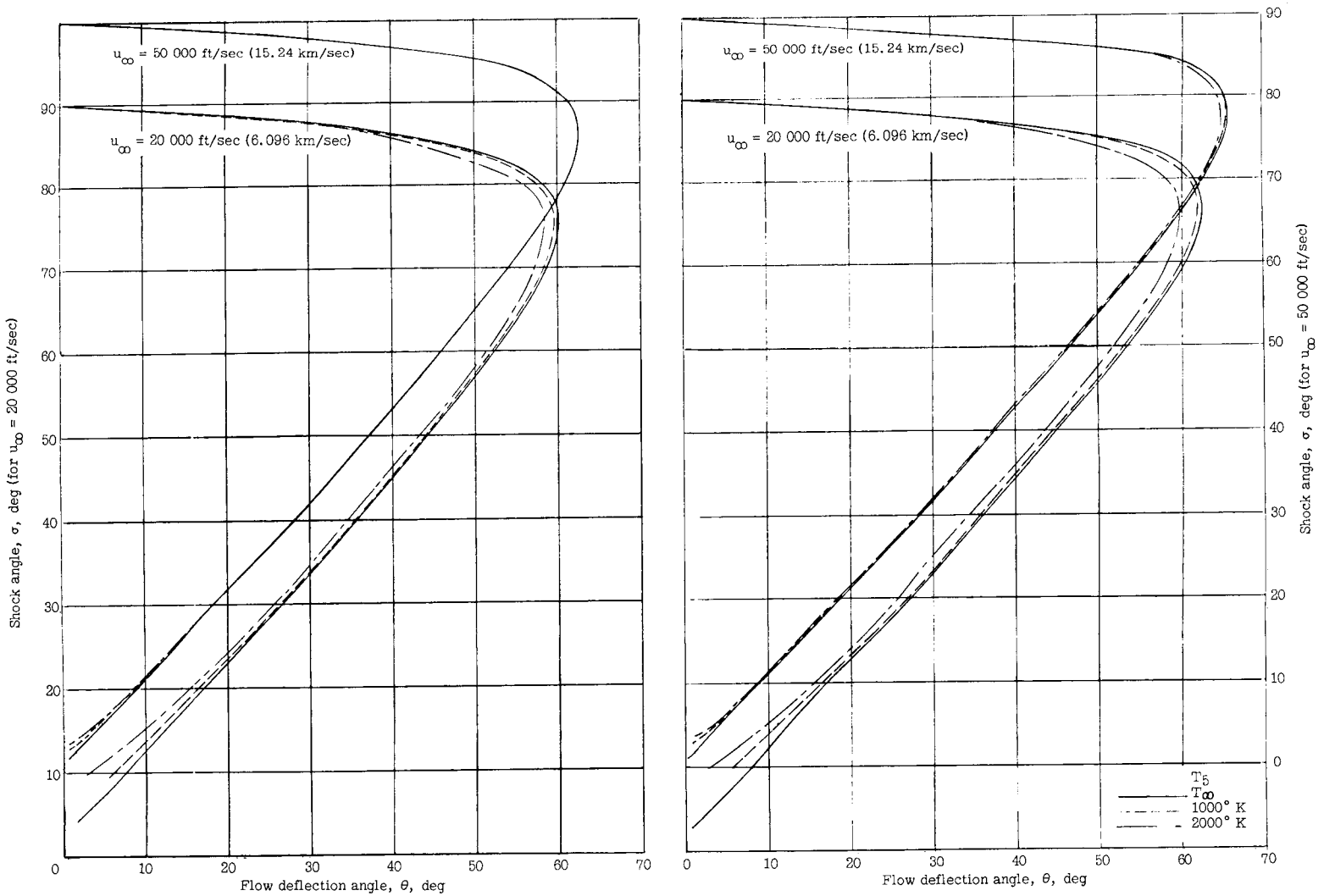

(a) Altitude = 200 000 ft (60.96 km).

(b) Altitude = 300 000 ft (91.44 km).

Figure 32.- Variation of shock wave angle with flow deflection angle across shock wave.

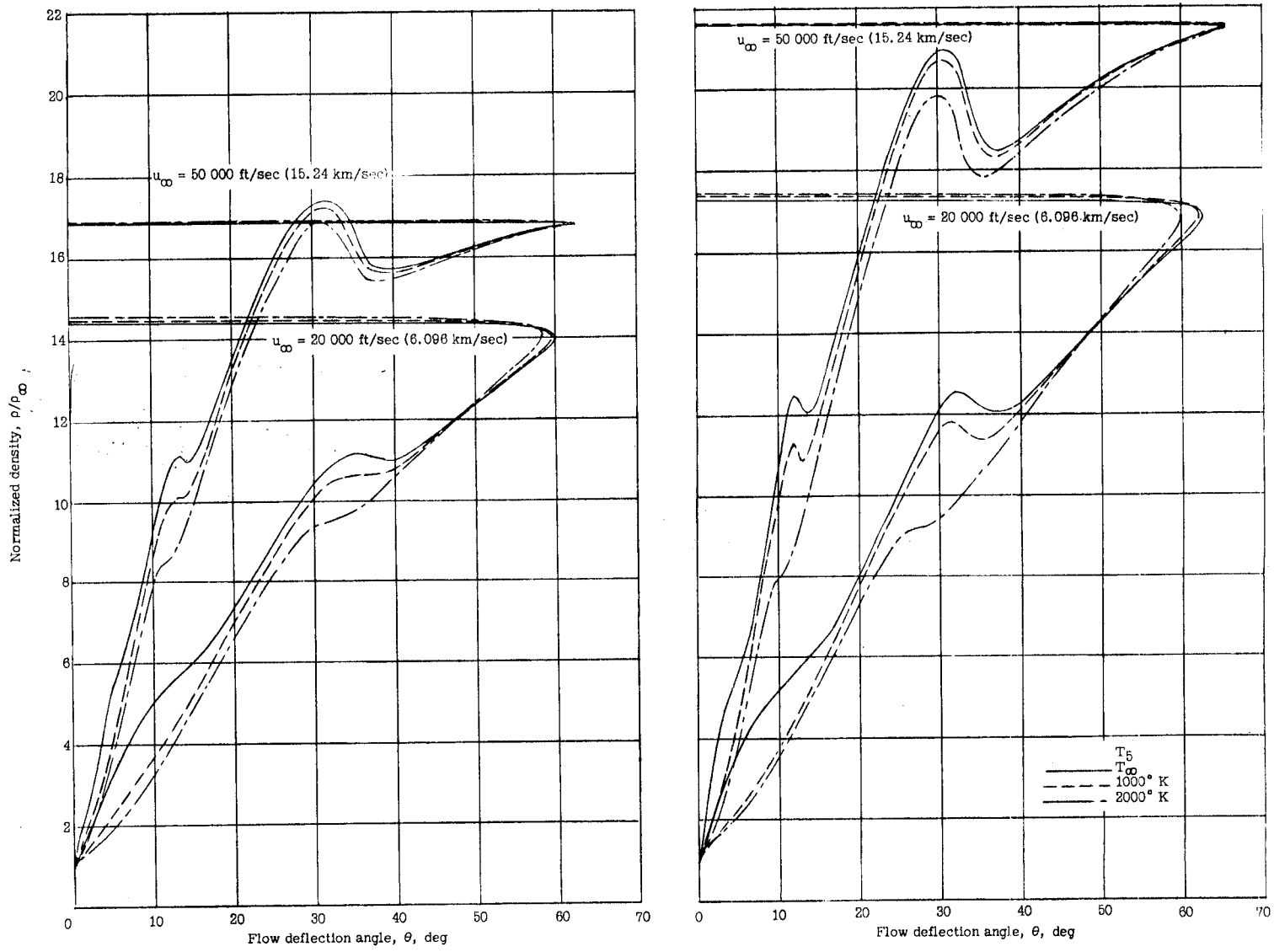

(a) Altitude = 200 000 ft (60.96 km).

(b) Altitude = 300 000 ft (91.44 km).

Figure 33.- Variation of normalized density behind shock wave with flow deflection angle across shock wave.

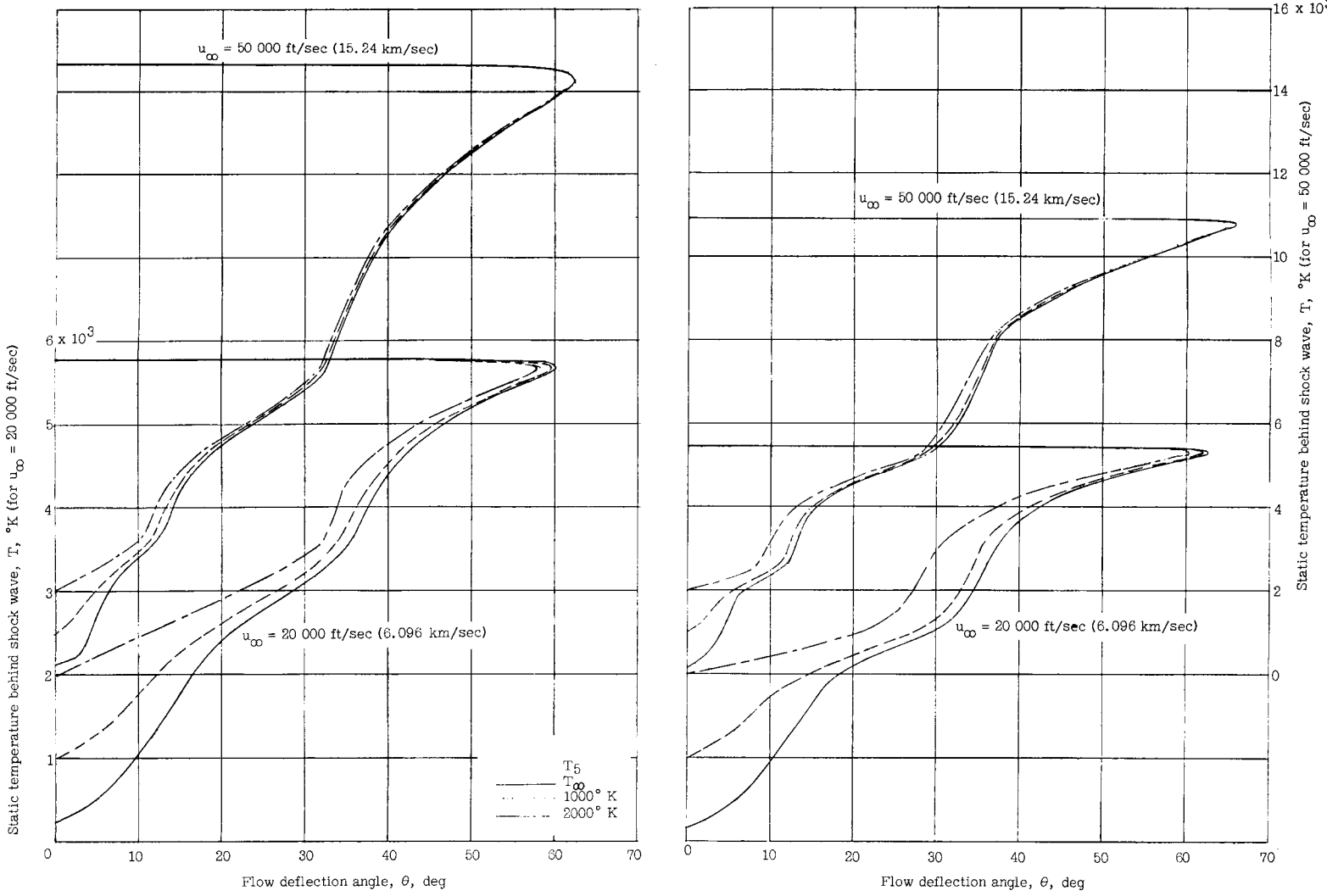

(a) Altitude = 200 000 ft (60.96 km).

(b) Altitude = 300 000 ft (91.44 km).

Figure 34.- Variation of static temperature behind shock wave with flow deflection angle across shock wave.

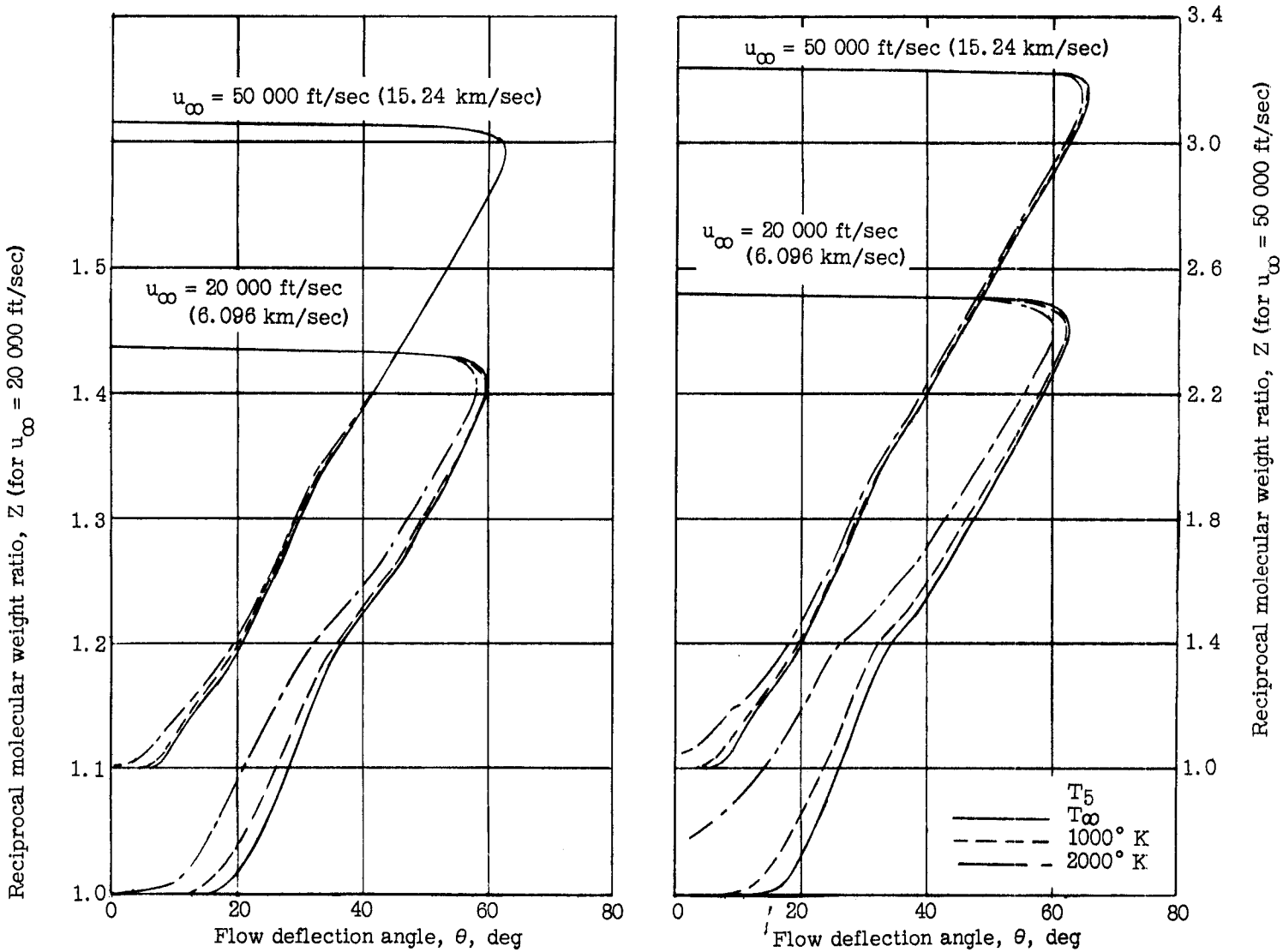

(a) Altitude = 200 000 ft (60.96 km).

(b) Altitude = 300 000 ft (91.44 km).

Figure 35.- Variation of reciprocal molecular weight ratio behind shock wave with flow deflection angle across shock wave.